Thesis for The Degree of LICENTIATE OF PHILOSOPHY

Single molecule Biosensing with Nanopores

Analyte Quantification & Electric-field Effects

AMINA SHAJI

Department of Chemistry and Chemical Engineering
Chalmers University of Technology
Gothenburg, Sweden, 2026

Single molecule biosensing with Nanopores

Analyte Quantification & Electric-field Effects

AMINA SHAJI

Licentiatuppsatser vid Institutionen för kemi och

kemiteknik Chalmers tekniska högskola.

Nr 2026:10

Department of Chemistry and Chemical Engineering
Division of Applied Chemistry
Andreas Dahlin Group
Chalmers University of
Technology SE-412 96
Gothenburg, Sweden Phone:
+46(0)31 772 1000

Supervisor – Prof. Andreas Dahlin

Examiner – Prof. Anette Larsson

Cover illustration: Schematics reproduced directly from two published articles included in this thesis. The left panel shows single-molecule analyte quantification using a solid-state nanopore, illustrating DNA translocation through a nanometer-scale membrane under an applied electric field. The right panel presents the effect of electric field on biotin-avidin interactions, comparing low and high voltages.

Printed by Chalmers Digitaltryck, Gothenburg, Sweden 2026.

"Every research goal hides something
Specific Measurable Achievable Realistic and Timely inside."

N anostructured
A perture for
N anoscale,
O ne molecule
P robing,
O bserving and
R evealing
E lectric field effects

"The PORE Story"
but not yet the *'hole'* story of my PhD.

Single molecule biosensing with Nanopores

Analyte Quantification & Electric-field Effects

AMINA SHAJI

Abstract

Solid-state nanopores enable label-free single-molecule analysis by converting the passage of analytes through the pore into electrical signals. This thesis examines quantitative analyte sensing with nanopores while addressing a central challenge: the exceptionally strong electric field in thin solid-state pores.

The first part of the work demonstrates that analyte concentration can be extracted directly from the voltage dependence of translocation event frequency. For double-stranded DNA in sufficiently large pores, the event frequency increases linearly with voltage. By extending measurements to high bias and introducing robust signal-processing routines for unstable baselines, the study establishes a calibration-free approach for concentration determination from nanopore data.

The second part demonstrates that the electric field inside a solid-state nanopore is not merely a passive readout mechanism, but rather a perturbative environment that actively modifies biomolecular interactions. Using the biotin-avidin interaction as a model system, applied bias shortens the effective lifetime of this strongly bound complex by several orders of magnitude. This finding has critical implications for affinity-based nanopore sensing, because binding kinetics measured in the pore can deviate substantially from field-free conditions.

The thesis further includes studies on thermoresponsive PNIPAM-grafted nanostructures for trapping enzymes and controlling ionic transport, which demonstrates the viability of developing integrated platforms that simultaneously provide electrical detection, optical readout, and dynamically gated access to confined biomolecules, enabling real-time monitoring of individual enzyme kinetics in controlled nanoscale environments.

Overall, these studies establish solid-state nanopores as versatile platforms for quantitative single-molecule biosensing, while revealing critical field-induced effects that must be considered in future bioanalytical applications.

Keywords: solid-state nanopores; single-molecule biosensing; analyte quantification; electric-field effects; biotin-avidin dissociation; PNIPAM gated nanostructures.

List of Publications

Appended publications

This thesis is based on the two appended publications – Paper I and Paper II, and additional peer reviewed articles from my earlier research is included in Other Publications.

Paper I

Solid-State Nanopore Sensors: Analyte Quantification by Event Frequency Analysis at High Voltages
Julia Järlebark, Wei Liu, Amina Shaji, Jingjie Sha, and Andreas Dahlin
Analytical Chemistry 2025 97 (8), 4359-4364
DOI:10.1021/acs.analchem.4c05037

Author contributions: performed nanopore measurements and contributed to the analysis of experimental data.

Paper II

The Electric Field in Solid State Nanopores Causes Dissociation of Strong Biomolecular Interactions
Wei Liu, John Andersson, Julia Järlebark, Amina Shaji, Jingjie Sha, and Andreas Dahlin
Nano Letters 2025 25 (24), 9654-9661
DOI:10.1021/acs.nanolett.5c01447

Author contributions: performed the SPR measurements and carried out the analysis of the SPR data.

Other publications

These following additional publications are from my pre-doctoral research, prior to the present PhD project.

1) *Assembly of Transmembrane Pores from Mirror-Image Peptides*
   Smrithi R. Krishnan, Kalyanashis Jana, **Amina Shaji**, Karthika S. Nair, Anjali Devi Das, Devika Vikraman, Harsha Bajaj, Ulrich Kleinekathöfer, and Kozhinjampara R. Mahendran

   Nature Communications 2022 13 (1), 5377 DOI: 10.1038/s41467-022-33155-6

   Authorship – Equally contributing first author. My contributions included determining the biophysical properties of the peptides, analyzing the single-channel recordings, and co-writing and approving the final manuscript.

2) *Designed Alpha-Helical Barrels for Charge-Selective Peptide Translocation*
   Smrithi R. Krishnan, Neethu Puthumadathil, **Amina Shaji**, K. Santhosh Kumar, Gayathri Mohan, and Kozhinjampara R. Mahendran
   Chemical Science 2021 12 (2), 639–649 DOI: 10.1039/D0SC04856

   Authorship – Second author. I contributed to the experimental work and data analysis on alpha-helical peptide pores, and to the writing, revision, and approval of the manuscript.

Acknowledgments

This PhD journey has been a deeply meaningful chapter in my life, shaped by the guidance, support, and kindness of many wonderful people. I owe this accomplishment to all those who stood by me and made it possible in countless ways.

First and foremost, I sincerely acknowledge the **European Commission (EC)** for the generous financial support. The freedom and resources provided through EC funding have been instrumental in enabling and enriching the research presented in this thesis.

I would like to express my profound and deepest gratitude **to my guiding light, Prof. Andreas Dahlin**, for his guidance, mentorship, and unwavering support throughout my doctoral journey so far. His scientific insight, encouragement, and trust continue to inspire and help me grow as both a researcher and an independent thinker as I advance toward the next stages of my PhD work. I am also thankful to my doctoral committee – **Prof. Fredrik Westerlund**, the co-supervisor, **Prof. Anette Larsson** the examiner and **Prof. Lars Öhrström**, the director of studies for their time, thoughtful evaluation, and constructive feedback, which have been invaluable in shaping this work and guiding my continued progress toward the PhD.

I feel incredibly fortunate to be part of such a **supportive and vibrant research group**. My sincere thanks go to my present and former wonderful group members **Bagus, Hao, Jesper, John, Julia, Maria, Sevil, Wei, and Zheng** for their inspiring discussions, teamwork, and the countless moments of laughter and encouragement that makes everyday lab life and office life enjoyable, pleasant and meaningful! 😍

I would also like to thank everyone at the **Applied Chemistry division** for creating such a supportive, friendly, and inspiring working environment. Special thanks to **Savitha** for helping me settle in at the beginning, and to **Nasim** and **Nivedhita** for the many enjoyable fika, thoughtful conversations, and genuine camaraderie that brightened even the most demanding days. 😊

My thanks go to my office mates **Åke, Sami, Arvindh, Luigi** whose friendly presence and daily support make working hours far more pleasant.

Beyond academia, I owe everything to my most **beloved family**! A very special and tender place in my heart is reserved for my beloved **Dad**, watching over me from heaven, and my dearest **Grandma**, Ummicha.. Her recent passing has left an irreplaceable void in my life. Although she could not witness my licentiate, her love, blessings, and unwavering belief in me continue to guide me every day. This milestone is deeply dedicated to her loving memory.

To my **Mommy love**, whose unconditional love, strength, and sacrifices have been my backbone; to my **Achukutta** for his constant support, love and belief in me; and to my little princess **Zoey the sunshine**, who is a source of comfort, joy, and calm during even the most stressful times - you mean the world to me! 😍

I am deeply grateful to my dearest **Baseema** and **Visakh chetta** for their unwavering love, encouragement, and support from afar - for everything - and to **Sami** here in Sweden. Thank you for standing by me through every high and low, celebrating my successes, and lifting me during difficult moments! 😍

I wish to acknowledge all my **former mentors and well-wishers** who have shaped my path in ways big and small. Your guidance, encouragement, and belief in me have carried me further than you may know.

Finally, my heartfelt thanks to **you**, the reader, for taking the time to read this work.

This thesis is not mine alone - it is a reflection of the love, support, and collective effort of everyone mentioned here and many more who walk with me, even from afar!

Abbreviations and chemical terms

Abbreviation	Expanded form	Use in the thesis
AFM	Atomic Force Microscopy	**Surface-topography characterization method for polymer brushes or nanostructures.**
Ag/AgCl	Silver/silver chloride	**Reference/electrode material used for applying voltage and measuring ionic current.**
APS	3-aminopropylsilatrane	**Silanization reagent used to introduce amine groups on SiNx/silica-type surfaces before PEG coupling.**
ARGET-ATRP	Activators Regenerated by Electron Transfer Atom Transfer Radical Polymerization	**Surface-initiated polymerization route used for PNIPAM brush growth.**
ATRP	Atom Transfer Radical Polymerization	**Controlled radical polymerization strategy for growing polymer brushes.**
CDB	Controlled Dielectric Breakdown	**Nanopore fabrication method in which an electric field locally breaks down a SiNx membrane.**
$CuBr_2$	Copper(II) bromide	**Copper catalyst precursor used in PNIPAM brush polymerization chemistry.**
DNA	Deoxyribonucleic acid	**Model nucleic-acid analyte used for nanopore translocation and event-frequency analysis.**
dsDNA	Double-stranded DNA	**Double-helical DNA; 2 kbp and 3 kbp dsDNA are used as model analytes in the thesis.**
EBL	Electron-beam lithography	**Nanofabrication method used for patterned nanowells/nanostructure arrays.**
EDTA	Ethylenediaminetetraacetic acid	**Chelating agent included in TE buffer to bind divalent metal ions and stabilize nucleic acids.**
EMCR	Elements EMCR software/interface	**Software/interface used with Elements nanopore amplifiers for current recording, voltage control, and data acquisition.**

FDG	Fluorescein di-beta-D-galactopyranoside	**Fluorogenic substrate for beta-galactosidase; cleavage releases fluorescent fluorescein.**
FFT	Fast Fourier Transform	**Signal-processing method used for filtering high-voltage nanopore traces and correcting slow baseline drift.**
FIB	Focused Ion Beam	**Top-down fabrication/milling method for solid-state nanopores.**
IPA	Isopropanol / isopropyl alcohol	**Solvent used for membrane wetting and cleaning/rinsing steps.**
I-V	Current-voltage	**Electrical characterization curve used to assess conductance, Ohmic behavior, and pore stability.**
KCl	Potassium chloride	**Electrolyte used in nanopore fabrication, conditioning, and ionic-current measurements.**
LCST	Lower Critical Solution Temperature	**Temperature near which PNIPAM switches between hydrated/extended and collapsed states.**
LiCl	Lithium chloride	**Electrolyte used during pore conditioning/enlargement in the experimental protocol.**
Me_6TREN / Me_6Tren	Tris[2-(dimethylamino)ethyl]amine	**Ligand used in ATRP/SARA-type polymerization chemistry for PNIPAM brushes.**
NH_4OH	Ammonium hydroxide	**Base component used in RCA-1/TL-1 cleaning chemistry.**
NIPAM	N-isopropylacrylamide	**Monomer polymerized to form PNIPAM thermoresponsive brushes.**
NMP	Nitroxide-mediated polymerization	**Controlled/living radical polymerization method mentioned as a brush synthesis strategy.**
PBS	Phosphate-buffered saline	**Physiologically relevant buffer used for more stable PNIPAM conductance measurements.**
PEG	Poly(ethylene glycol)	**Neutral polymer used for surface passivation and as a**

		non-thermoresponsive control brush.
PIMP	Photoiniferter-mediated polymerization	**Surface-initiated polymerization method mentioned in the polymer-brush synthesis overview.**
PMDETA	N,N,N',N'',N''-pentamethyldiethylenetriamine	**Ligand used in SI-ARGET-ATRP chemistry for PNIPAM brush growth.**
PNIPAM	Poly(N-isopropylacrylamide)	**Thermoresponsive polymer brush used for gated nanostructures and ion-transport studies.**
RAFT	Reversible Addition-Fragmentation Chain Transfer polymerization	**Controlled radical polymerization strategy mentioned for polymer-brush synthesis.**
RNA	Ribonucleic acid	**Biomacromolecule introduced in the thesis background as a biological analyte class.**
RPS	Resistive Pulse Sensing	**Nanopore sensing principle based on transient current changes caused by single particles or molecules.**
SAM	Self-assembled monolayer	**Organized molecular layer formed on gold/palladium surfaces for surface functionalization.**
SARA	Supplemental Activators and Reducing Agents	**Polymerization approach tested for PNIPAM brush growth using copper-based chemistry.**
SiNx	Silicon nitride	**Thin solid-state membrane material used for nanopore fabrication.**
SiO_2	Silicon dioxide / silica	**Substrate or surface material in nanostructures and adsorption/washing discussions.**
SIP	Surface-initiated polymerization	**Grafting-from approach where polymer chains grow from initiators attached to a surface.**
SMCC	Sulfosuccinimidyl 4-(N-maleimidomethyl)cyclohexane-1-carboxylate	**Bifunctional crosslinker used after APS functionalization for PEG grafting.**

SPR	Surface Plasmon Resonance	**Label-free optical technique used for polymer-brush characterization and field-free binding controls.**
TEM	Transmission Electron Microscopy	**Top-down nanopore drilling/imaging method discussed for solid-state nanopore fabrication.**
TE	Tris-EDTA buffer	**Buffer used with DNA samples; typically contains Tris and EDTA.**
XPS	X-ray Photoelectron Spectroscopy	**Surface-chemical characterization method for confirming composition and functionalization.**
beta-gal / beta-galactosidase	beta-galactosidase	**Model enzyme used in PNIPAM-gated nanowell confinement and FDG fluorescence readout.**
H_2O_2	Hydrogen peroxide	**Oxidizing reagent used in piranha and RCA-1 cleaning solutions.**
H_2SO_4	Sulfuric acid	**Acid component of piranha cleaning solution.**
H_2O	Water	**Solvent and buffer component used throughout sample preparation and polymerization protocols.**
Tris	Tris(hydroxymethyl)aminomethane	**Buffer component in TE buffer.**
Au	Gold	**Nanostructure material compatible with thiol-based SAM formation.**
Pd	Palladium	**Nanostructure material used for enzyme confinement; may require oxide reduction before thiol chemistry.**
PdO	Palladium oxide	**Surface oxide that can hinder thiol binding on palladium nanostructures.**
Cr	Chromium	**Adhesion layer used below gold/palladium films in nanostructure fabrication.**
A. oryzae	Aspergillus oryzae	**Source organism for the beta-galactosidase enzyme used in confinement experiments.**

E. coli	Escherichia coli	**Common bacterial beta-galactosidase source used for comparison in the thesis discussion.**
MW	Molecular weight	**Used to describe enzyme or analyte size, for example beta-galactosidase.**
kbp	Kilobase pairs	**Unit of double-stranded DNA length; 3 kbp means approximately 3000 base pairs.**
kDa	Kilodalton	**Unit of molecular mass used for proteins and polymers.**
nM	Nanomolar	**Concentration unit used for DNA/protein working solutions.**
pH	Potential of hydrogen	**Measure of solution acidity/basicity; used in enzyme loading and washing conditions.**

Common symbols and measurement variables

Abbreviation	Expanded form	Use in the thesis
c	Analyte concentration	**Used in event-frequency and concentration quantification models.**
D	Diffusion coefficient / diffusivity	**Transport parameter; compared with electrophoretic mobility in capture models.**
d	Pore diameter	**Key geometric parameter controlling conductance and molecular blockade.**
G	Conductance	**Electrical conductance of the open or modified nanopore.**
I_0	Open-pore current	**Baseline current through the nanopore without an analyte in the pore.**
$\Delta I / I_0$	Fractional current blockade	**Normalized blockade depth produced by analyte translocation or binding.**
f	Event frequency	**Number of nanopore events per unit time; central observable for concentration readout.**
f(V)	Event frequency as a function of voltage	**Voltage-dependent frequency curve used for calibration-free quantification.**
l	Pore length / membrane thickness	**Geometric parameter in conductance and field models.**
R	Resistance	**Inverse of conductance; includes pore and access resistance contributions.**
Tau, τ	Dwell time	**Duration of a translocation or binding event in the nanopore signal.**
Mu, μ	Electrophoretic mobility	**Transport parameter controlling field-driven capture in the diffusion-limited model.**
Sigma, σ	Electrolyte conductivity	**Solution property used in conductance calculations.**
Chi, χ	Flory interaction parameter	**Polymer-solvent parameter used to describe PNIPAM brush swelling/collapse.**
ΔU / V	Applied voltage / bias	**Electrical driving force applied across the nanopore membrane.**
°C	Degrees Celsius	**Temperature unit used for LCST, enzyme loading, and conductance experiments.**

Contents

Appended papers

Paper I

Paper II

Part I

Summary

Part I presents an overview of the thesis, covering the introduction, background theory, experimental methods, key results from the two appended papers, relevant unpublished results, and the concluding outlook.

- Introduction
- Theory
- Experimental methods
- Summary of Papers I & II
- Unpublished results
- Concluding outlook

Chapter 1

Introduction

1.1 Nanopores – as artificial analogues of biological systems

Life is sustained by the tightly regulated movement and exchange of essential chemical building blocks and signaling molecules that maintain cellular structure and function, thereby keeping the cells alive and functioning in the living system[1]. These include inorganic ions such as sodium, potassium, calcium, chloride, and magnesium which generate ionic gradients and differences in electric potential required for nerve impulse transmission, muscle contraction, and the regulation of cell volume[2–5]. Cells also rely on metabolites, including glucose, amino acids, and adenosine triphosphate (ATP), to provide energy and molecular substrates for growth, repair, and intracellular signaling[6]. In addition, biomacromolecules such as the membrane that act as gates, which open and close in response to DNA, RNA and proteins as well as their shorter fragments such as oligonucleotides and peptides are central to the storage and transmission of genetic information and to structural and enzymatic functions respectively[7]. These movements of biomolecules are not random; they are strictly regulated[*] by protein channels or pores in signals so the cell can maintain an order in a crowded molecular environment[8,9].

From a technological and scientific perspective, artificial nanopores were developed to mimic and exploit this biological principle at the single-molecule level[10]. In a nanopore experiment, the motion or binding of an individual molecule inside a nanometer-scale aperture is converted into an electrical signal, which

---

[*] ***Life regulates ions and biomolecules through nanoscale gates; nanopores translate this principle into single-molecule sensing.***

makes it possible to study transport and interactions one event at a time. Conventional analytical techniques measure ensemble averages and lack the resolution to observe individual molecules in real time. The need to observe individual molecules in real time arises from the inherent heterogeneity and dynamic behavior of biological systems, which are often obscured by ensemble-averaged measurements[11]. While bulk techniques have been instrumental in identifying average structures, reaction pathways, and intermediate states - they mask stochastic fluctuations, transient conformations, and rare events that can be critical to function. For example, Ferritin, a spherical iron storage molecule which is also explored as a targeted drug delivery carrier, has been extensively studied using ensemble methods that identify structural intermediates in its disassembly and reassembly pathways. These measurements provide snapshots and average populations of intermediates, but they do not resolve how individual ferritin molecules fluctuate between states or how heterogenous their disassembly and reassembly trajectories are in real time. Therefore, single-molecule approaches are essential to reveal how ferritin responds to different environments, enhancing its efficacy as a nanocarrier for drugs and bioactive molecules. This approach offers information by revealing molecules to molecules variability and rare pathways that are hidden in bulk averages[12].

Single-molecule approaches overcome the limitations of bulk measurements by directly probing molecular-level dynamics, enabling the resolution of pathway diversity, kinetic variability, and structure–function relationships. Such measurements are essential for understanding processes such as protein folding and conformational switching, nucleic acid translocation and hybridization, enzyme catalysis, molecular recognition, and the operation of molecular motors. By capturing real-time dynamics at the level of individual entities, single-molecule techniques provide mechanistic insight that is inaccessible to ensemble methods and are therefore crucial for advancing applications in biotechnology, medicine, and nanotechnology[13,14].[*]

---

[*] **Conventional analytical methods measure millions of molecules together and report only average signals.**

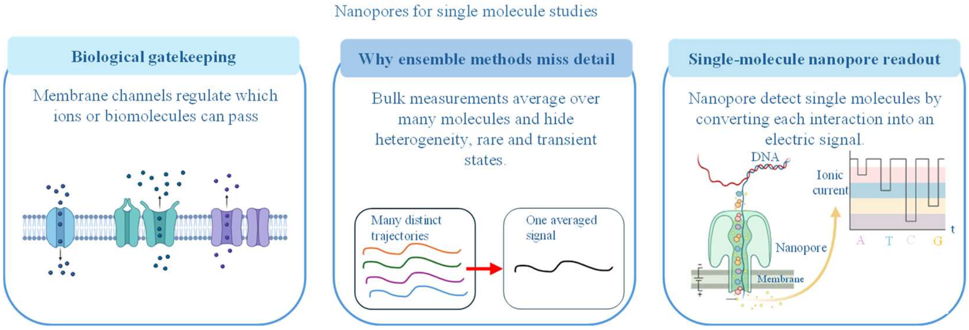

Figure 1 - Introduction to nanopore bioanalysis

Advancements in nanotechnology have enabled the development of powerful single-molecule sensing techniques that probe the physical and chemical properties of biomolecules with unprecedented precision. Among these, nanopore-based electrical sensing has emerged as a versatile platform for detecting and studying the binding kinetics of the analytes from ionic current signatures as they translocate through a nanoscale pore. This approach offers high temporal resolution, label-free detection, and compatibility with a wide range of analytes including nucleic acids, proteins etc, positioning it as a promising tool for applications in diagnostics, molecular biology, and biosensing[15,16].

1.2 From natural pores to artificial nanopores

In biological membranes, protein channels and pores decide which molecules may enter or leave a cell, and under what conditions. Some pores let ions pass rapidly but only of a particular type, while others transport larger molecules such as sugars or nucleic acids[8,17] often with the aid of specific carrier proteins or channel proteins termed as the shuttle cargo mechanism[18]. At a basic level, all of them implement a simple principle: a tiny opening that is selective and controllable. Nanopore sensing takes this simple principle and recreates it in an artificial, yet highly controlled setting.

Nanopores[*] exist in several distinct implementations, all based on the same fundamental principle: a nanometer-scale aperture that acts as selective gates for ions and molecules, only certain species or sizes can pass, and their passage is detected by the change in ionic current. Nanopores are commonly classified into biological, solid-state, and hybrid or functionalized systems, each

---

[*] **Nanopore sensing mimics nature's selective transport through membrane channels.**

implementing a nanoscale aperture that acts as a selective gate for ions and molecules with passage detected via changes in ionic current[*].

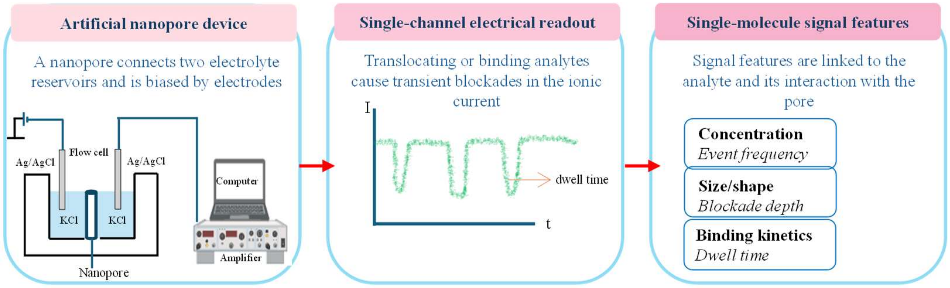

Figure 2 - Overview of nanopore sensing

1.2.1 Biological nanopores

Biological nanopores are protein-based channels that naturally span lipid bilayers, including well-studied examples such as α- hemolysin[19], MspA[20], and aerolysin[21]. These pores are genetically encoded and self-assemble into highly uniform structures with atomically precise dimensions and defined chemical functionalities, such as charge distributions, binding motifs, and gating domains[22]. In sensing applications, an individual protein pore is reconstituted into a lipid membrane, and the ionic current through the pore is measured. Translocation or binding of analytes such as DNA, peptides, or small molecules produces characteristic and highly reproducible current modulations due to the structural identity of each pore. The biological nanopores exhibit exceptional structural uniformity and well-defined surface chemistry and have high sensitivity and favorable signal-to-noise ratios at relatively low operating voltages.

---

[*] **Nanopore sensing is label-free: we read molecules directly, without fluorescent tags or special dyes attached.**

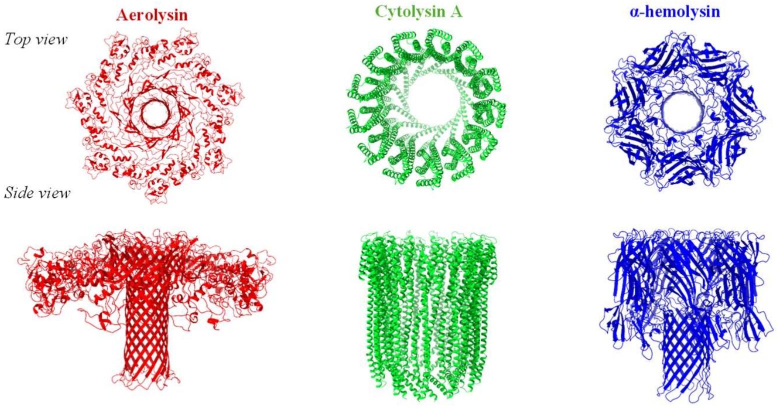

Figure 3 - Biological nanopores widely used in single-molecule sensing[*]

However, they are limited by operational stability with respect to temperature, voltage, and solvent conditions. They have restricted geometric tunability, with modifications typically requiring protein engineering or chemical functionalization. Moreover, extracting these membrane proteins from the biological system is tedious[23–26].

---

[*] **Biological nanopores provide atomically precise sensing apertures, but their stability and geometric tunability are limited.**

1.2.2 Solid-state nanopores

Solid-state nanopores are typically fabricated in thin inorganic membranes, such as silicon nitride, silicon dioxide, graphene, and other two-dimensional materials, using either top-down or bottom-up approaches. In top-down methods, including Transmission Electron Microscopy (TEM) drilling and Focused Ion Beam (FIB) milling, fabrication starts from a continuous solid film and material is removed locally to define a nanopore with precise control over pore diameter and membrane thickness. In addition to these top-down methods, Controlled Dielectric Breakdown (CDB) offers an alternative route in which an applied electric field induces local material degradation and pore formation within the membrane. In general, solid-state nanopores exhibit high mechanical robustness and chemical stability, allowing operation under a wide range of conditions, including high ionic strength, extreme pH, and elevated voltages. However, long-term stability can depend on the specific fabrication method; for example, pores formed by CDB may show more drift or need restructuring than pores sculpted by TEM or FIB, as reported in comparative studies[27,28]. The broad tunability of pore diameter, geometry, membrane thickness and straightforward integration with microfluidic platforms and on-chip electronic systems make them particularly attractive for sensing applications. For solid state nanopores, achieving atomic scale structural uniformity remains challenging leading to pore-to-pore variability. Also, unmodified surfaces often exhibit increased noise and nonspecific adsorption, necessitating surface functionalization[10,16,29].

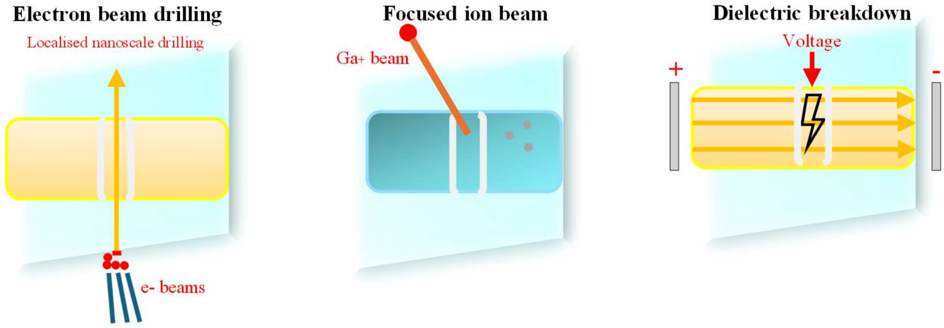

Figure 4 - Solid state nanopore fabrication methods[*]

---

[*] **Solid-state nanopores offer robust, tunable, and integrable nanostructures for label-free molecular detection.**

1.2.3 Hybrid and functionalized nanopores

Hybrid nanopores combine a biological or solid-state aperture with an additional functional layer, such as DNA origami, surface-bound receptors, proteins, or polymer coatings. These hybrid systems are attractive because they can merge the robustness of synthetic structures with the recognition, gating, or programmability of soft matter and biomolecular components. The advantages include the integration of the robustness of solid-state systems with the specificity and tunability of biological or synthetic components along with customizable selectivity, gating behavior, and responsiveness to external stimuli such as pH, temperature, or ligand binding. The major limitations are that the increased design and characterization complexity due to multiple interacting components, and the functional layers may introduce additional noise or instability if not carefully optimized[30,31].

Although nanopore experiments focus on one pore and one molecule at a time, the phenomena they probe are directly related to how biological systems function on larger scales. Instead of a protein channel in a cell membrane, one uses a nanometer-sized hole in a solid-state membrane or a single protein pore embedded in a synthetic bilayer. The geometry, surface chemistry, and driving forces can then be tuned deliberately, allowing one to study how individual molecules move through this simplified "artificial gate."[*]

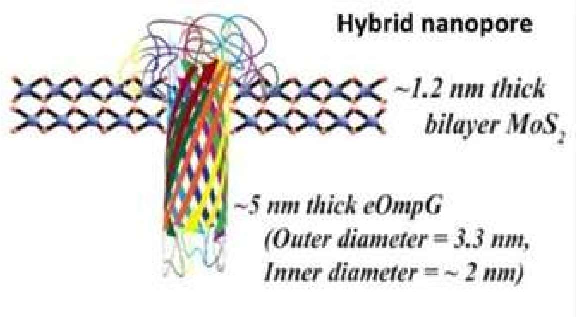

Figure 5 - Hybrid nanopore, Reproduced from[33]

---

[*] **Hybrid nanopores combine synthetic robustness with functional molecular recognition.**

1.2 Scope of this thesis

This thesis investigates how solid-state nanopores can be used for quantitative single molecule biosensing and how the strong electric field inside thin nanopores influences the biomolecular systems being measured. The work is guided by the following research questions and hypotheses.

Published results[*]

RQ1: Can analyte concentration be determined directly from voltage-dependent nanopore event frequency without an external calibration standard?

Hypothesis 1: For sufficiently large solid-state nanopores, where entry barriers are negligible, the event frequency scales linearly with applied voltage, and the slope of this relation is proportional to analyte concentration.

RQ2: Does the electric field in a solid-state nanopore perturb strong biomolecular interactions used for affinity-based sensing?

Hypothesis 2: The electric field can exert electrophoretic forces large enough to shorten the effective lifetime of strongly bound biotin-avidin complexes compared with field-free conditions measured by SPR.

---

[*] **This thesis asks how solid state nanopores can quantify analytes while accounting for electric field perturbation.**

Unpublished results[*]

RQ3: Can thermoresponsive PNIPAM-grafted nanostructures provide gated molecular access for single enzyme confinement?

Hypothesis 3: PNIPAM brushes can switch between hydrated and collapsed conformations to open and close nanocavities, thereby enabling controlled trapping and release of individual enzymes.

RQ4: How do thermoresponsive PNIPAM-grafted nanostructures influence ionic transport, and under what conditions can they be used for reliable conductance measurements?

Hypothesis 4: In the hydrated state, PNIPAM brushes permit ionic conductance by allowing ions to pass through the swollen brush layer, whereas sufficiently thick PNIPAM brushes can remain effectively nonconductive even in the collapsed state, blocking ion transport across the nanostructure.

Together, these questions define the central aim of the thesis: to develop nanopore-based sensing strategies that are quantitatively useful while identifying field induced effects that must be controlled in future bioanalytical devices.

---

[*] **This thesis also addresses how thermoresponsive PNIPAM-grafted nanostructures are employed for enzyme confinement and reliable ionic conductance readouts.**

Chapter 2

Theory

2.1 Resistive Pulse Sensing

Resistive pulse sensing (RPS) is an electrical technique in which individual analytes passing through a small, electrolyte filled aperture displace ions and transiently increase the resistance, producing a 'resistive pulse' in the ionic current.

The amplitude, duration, and shape of each pulse report on properties such as size, shape, and charge of the analyte, and the event frequency reflects its concentration[*]. A classical implementation is the Coulter counter, widely used for counting and sizing cells and particles, which inspired nanopore based RPS at the molecular scale. The evolution of RPS and nanopore sensing is shown in Figure 6.

Early developments in nanopore sensing relied heavily on biological nanopores, naturally occurring protein channels that offer apertures on the Ångström scale. Examples include α-hemolysin[32], voltage-gated ion channels[33], and genetically engineered pores[34]. Devices employing single biological pores,

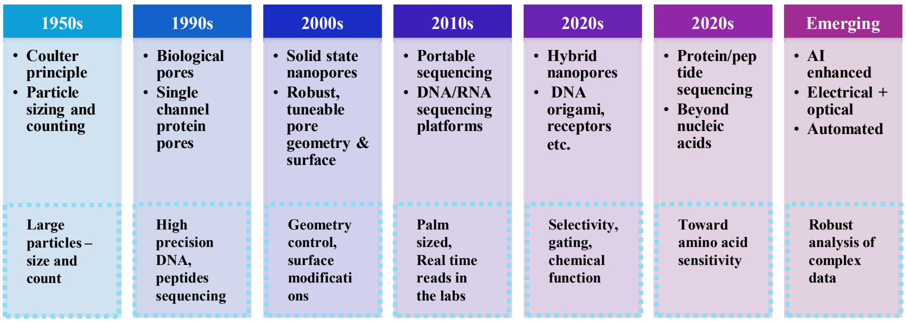

1950s	1990s	2000s	2010s	2020s	2020s	Emerging
• Coulter principle • Particle sizing and counting	• Biological pores • Single channel protein pores	• Solid state nanopores • Robust, tuneable pore geometry & surface	• Portable sequencing • DNA/RNA sequencing platforms	• Hybrid nanopores • DNA origami, receptors etc.	• Protein/peptide sequencing • Beyond nucleic acids	• AI enhanced • Electrical + optical • Automated
Large particles – size and count	High precision DNA, peptides sequencing	Geometry control, surface modifications	Palm sized, Real time reads in the labs	Selectivity, gating, chemical function	Toward amino acid sensitivity	Robust analysis of complex data

Figure 6 - Evolution of RPS and nanopore sensing

---

[*] **The amplitude, duration, and shape of each pulse report on properties such as size, shape, and charge of the analyte, and the event frequency reflects its concentration.**

most prominently α-hemolysin have demonstrated the remarkable ability to detect individual analyte-pore interactions, transducing these stochastic binding or translocation events into ionic current blockades[35–37]. Such current traces encode information about the analyte identity, concentration, and even molecular conformation, depending on pore design and conditions. Importantly, advances in protein engineering have further expanded the versatility of biological nanopores by enabling the tailoring of their selectivity and functionality for specific sensing tasks[38].

In parallel with biological pores, significant attention has been devoted to the development of solid-state nanopores which form the central focus of this thesis as robust synthetic analogues[34]. Fabricated in thin insulating membranes such as silicon nitride, silicon dioxide, or graphene, these nanopores can be precisely engineered using techniques such as focused ion beam milling[39,40], electron beam sculpting[41], or controlled dielectric breakdown[42]. Unlike biological pores, which are limited by their protein structure and stability, solid-state nanopores offer excellent mechanical robustness, full control over geometry, ability to withstand different environments and allowing pore diameters to be tuned from a few nanometeres to tens of nanometers[43,44]. Furthermore, their surfaces can be chemically functionalized[45], for example, with polymer brushes[46] or recognition elements to reduce nonspecific adsorption or to impart molecular specificity.

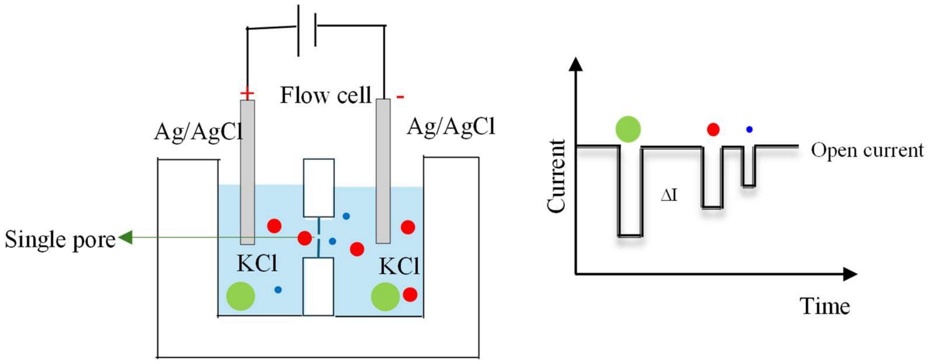

Figure 7 - RPS Left: Typical setup with two cells separated via an insulating membrane with a single pore. Right: Transient signal of current representing a large green, medium – sized red and small blue particle.*

---

* **Resistive pulse sensing converts molecular passage through a nanoscale aperture into transient current changes.**

2.1.1 Ionic current through a nanopore

In a nanopore experiment, an ionic current is driven through the pore by an applied voltage. When no molecule is present, the current is relatively steady and determined mainly by the pore size and the properties of the electrolyte. When a molecule enters or passes through the pore, it partially blocks or perturbs the ionic flow, causing a brief change in current. Each such event appears as a spike or dip in the recorded current trace as shown in figure 6.

These small perturbations are the key to nanopore sensing: each time a molecule interacts with the pore, that microscopic event is converted into a macroscopic electrical signal. By analyzing the frequency, depth, and duration of these events, it becomes possible to infer properties such as the concentration of the analyte, its size, charge, or even its sequence in the case of DNA and RNA. In this way, nanopores turn the invisible motion of single molecules into a stream of information that can be quantified.

An essential question in RPS* is how to model the conductance of nanopores. The conductance, defined as G = I/V (the reciprocal of resistance), where I is the ionic current and V is the applied voltage depends on both the geometry of the pore and the ionic conductivity of the solution. In the high-salt limit, where electrolyte concentrations are sufficiently large (typically >0.1 M) and the Debye length is much smaller than the pore diameter, the influence of surface charges on ion transport can be neglected[47]. Under these conditions, conductance is dominated by the bulk properties of the electrolyte and the geometry of the pore.

In Eq. (1), For a simple cylindrical pore, G is the open-pore conductance, σ is the electrolyte conductivity, d is the pore diameter, and l is the pore length, which is approximated by the membrane thickness, the conductance is given by:

$$G = \frac{\sigma\pi\, d^2}{4l} \qquad \text{(Eq.1)}$$

It highlights two key dependencies: (i) conductance increases quadratically with pore diameter and (ii) conductance decreases inversely with pore length, meaning

---

*** The Hall-type model links pore diameter, membrane thickness, electrolyte conductivity, and access resistance.**

that thinner membranes yield higher conductance for the same diameter.

When an electric potential is applied across a nanopore in an electrolyte, the steady-state current is limited by two serial contributions[*]:

(i) the internal pore resistance associated with ion transport through the pore lumen, and (ii) the access resistance that arises from the geometric convergence of current lines into the pore entrance and their divergence upon exit. The access term was first derived analytically for a circular aperture by Hall, who showed that it is independent of bulk cell size and scales inversely with aperture size[48]; for thin solid-state membranes, it can constitute a significant (often dominant) fraction of the total resistance[49].

2.2.1 Cylindrical nanopore

The corresponding internal (channel) resistance is simply the inverse of Equation 1:

$$R_{pore} = \frac{4l}{\sigma\pi d^2} \qquad \text{(Eq.2)}$$

The access resistance originates from hemispherical current spreading on each side of a circular aperture. For a circular aperture of diameter d, the per-side access resistance is

$$\frac{1}{2\sigma d};$$

therefore, for a free-standing membrane with two identical sides, the total access resistance is

$$R_{access} = \frac{1}{\sigma d} \qquad \text{(Eq.3)}$$

Consequently, the total resistance and conductance (Hall model) are

$$R_{total} = \frac{4l}{\sigma\pi\ \ ^2} + \frac{1}{\sigma d} \qquad \text{(Eq.4)}$$

$$G = \left(\frac{4l}{\sigma\pi d^2} + \frac{1}{\sigma d}\right)^{-1} \qquad \text{(Eq.5)}$$

---

[*] **Nanopore conductance reflects both transport through the pore and current convergence near the pore mouth.**

These expressions reduce to the familiar quadratic $G \propto d^2$dependence when $l \gg d$(pore term dominates), but they exhibit a nearly linear $G \propto d$ scaling in the thin-membrane limit where the access term becomes comparable to or larger than the pore term behaviour broadly documented for solid-state nanopores[50].

The Hall access resistance expressions above serve as a reference model for uncharged (weakly charged) nanopores in high salt electrolytes, where ion transport is dominated by the bulk solution and the current -voltage response is Ohmic. At low ionic strengths or for strongly charged membranes (e.g., SiN_x/SiO_2), additional effects such as surface conduction along the charged walls and concentration polarization - the formation of ion depleted and ion enriched regions near the pore due to ion selectivity can modify the effective conductance and its salt dependence[51–54]; in such regimes, extended models or corrections to the Hall model are necessary.

2.2.2 Conical (truncated - cone) nanopore

Many fabrication routes in particular CDB and some focused ion or electron beam sculpting protocols produce pores better approximated as truncated cones[*] rather than perfect cylinders. Let's denote the small opening diameter d_s, the large opening diameter d_l, the membrane thickness l, and the electrolyte conductivity σ. Integrating the local resistive contribution along the axis for a linearly varying cross-section yields the internal pore resistance;

$$R_{\text{pore}} = \frac{4\,l}{\sigma\,\pi\,d_s d_l}, \quad \text{(Eq.6)}$$

which reduces continuously to the cylindrical formula when $d_s = d_l = d$. In practice, the access resistance of a conical pore is dominated by the narrow opening (the primary current constriction), so a widely used and accurate approximation for symmetric bulk conditions is

$$R_{\text{access}} \approx \frac{1}{\sigma d_s} \qquad \text{(Eq.7)}$$

---

[*] **Conical nanopores are controlled mainly by the narrow opening, which strongly influences total resistance.**

Accordingly, the total resistance and conductance are:

$$\boxed{R_{\text{total}} = \frac{4\,l}{\sigma\,\pi\,d_s d_l} + \frac{1}{\sigma d_s}, G = \left(\frac{4\,l}{\sigma\,\pi\,d_s d_l} + \frac{1}{\sigma d_s}\right)^{-1} \qquad \text{(Eq.8)}}$$

This conical model captures the experimentally observed reduction of resistance relative to a same-length cylinder and highlights that, for a truncated cone, the smaller opening d_s largely controls the overall conductance through its appearance in both R_{pore} and R_{access}. More detailed analytical and numerical treatments for hourglass or cone-shaped nanopores, together with experimental studies on solid-state pores, confirm that these simple expressions describe the Ohmic conductance very well in the high-salt, weakly charged regime.

2.3 Asymmetry and surface-charge effects

Geometric asymmetry (e.g., pores that taper between two different diameters rather than being symmetric cylinders) combined with nonuniform surface charge distributions are well known to produce ion-current rectification, in which the current - voltage characteristics become diode-like[55,56]. This rectification[*] is often strongest at low to moderate ionic strength, where Debye layers (are thick enough to) strongly modulate the local conductivity, and it is particularly pronounced in short or ultrathin membranes where access and interfacial effects dominate. The classical Hall type (access-plus-pore) Ohmic conductance model, which assumes symmetric geometry, uniform conductivity, and linear response, can therefore break down when surface charge, double-layer overlap, or strong geometric asymmetry introduce nonlinear ion transport and spatially varying ion concentrations near the pore[55]. In such regimes - characterized by low ionic strength, strong surface charge, ultrathin membranes, or pronounced tapering - continuum electrokinetic models based on the Poisson - Nernst - Planck equations (often combined with Poisson - Boltzmann descriptions of the double layer) are

---

[*] **Geometry, surface charge, and ion distributions can produce nonlinear conductance and ion-current rectification.**

typically employed to capture ion-current rectification, concentration polarization, and other nonlinear current - voltage behaviour[57].

2.4 Analyte induced conductance modulation

Having established the open-pore conductance in the absence of an analyte, one can consider how the introduction of an analyte modulates the ionic conductance. As a first approximation, the analyte is treated as an ion-excluding object: it occupies part of the pore volume and thereby reduces the number of charge carriers available for conduction. In this volume-exclusion picture, the instantaneous conductance decreases by an amount $\Delta G \equiv G_0 - G_\mathrm{a}$, where $G_0$and $G_\mathrm{a}$denote the open-pore and analyte-occupied conductances, respectively.

2.4.1 Channel - only (volume - exclusion) model

If access resistance is neglected and the analyte is approximated as a cylinder with cross-section diameter $d_\mathrm{a}$and length much greater than the membrane thickness ($L_\mathrm{a} \gg l$), the analyte simply removes the area $\frac{\pi d_\mathrm{a}^2}{4}$ from the conducting cross-section. Under this approximation, the blockade amplitude is

$$\Delta G = \sigma \frac{\pi d_a^2}{4l} \qquad \text{(Eq.9)}$$

This model captures the intuitive result that the blockade scales with the analyte's cross-sectional area and, within the channel-only assumption, is independent of the pore diameter.

2.4.2 Pore-size dependence via access resistance (Hall model insertion)

In thin solid-state membranes, the access resistance can constitute a substantial part of the total resistance, particularly for pores that are not extremely small. Under these conditions, the conductance blockade

$$\Delta G = G_0 - G_a$$

is influenced both by the analyte cross-section and by the pore diameter d. Following the approach used in reference[58] describe the open-pore conductance with the Hall expression for a cylindrical nanopore of effective diameter d:

$$G_0 = \left(\frac{4l}{\sigma\pi d^2} + \frac{1}{\sigma d}\right)^{-1} \qquad \text{(Eq. 10)}$$

In the volume-exclusion[*] model, the analyte is treated as an ion-excluding cylinder (e.g. dsDNA) that occupies part of the pore lumen but does not alter the access resistance. The analyte reduces only the conducting cross-section inside the pore, so the effective channel diameter becomes,

$$\tilde{d} = \sqrt{d^2 - d_a^2}$$

where $d_a$is the analyte diameter. The conductance in the presence of analyte is then,

$$G_a = \left(\frac{4l}{\sigma\pi(d^2 - d_a^2)} + \frac{1}{\sigma d}\right)^{-1} \qquad \text{(Eq. 11)}$$

and the corresponding blockade amplitude, including access resistance is,

$$\Delta G = G_0 - G_a = \left(\frac{4l}{\sigma\pi d^2} + \frac{1}{\sigma d}\right)^{-1} - \left(\frac{4l}{\sigma\pi(d^2 - d_a^2)} + \frac{1}{\sigma d}\right)^{-1} \text{(Eq. 12)}$$

In the channel-dominated limit ($l \gg d$), the access term $1/(\sigma d)$ becomes negligible and Eqs. 11–12 reduce to the familiar channel-only expressions, for which the blockade depends primarily on the analyte cross-section and only weakly on pore diameter. This is the regime where $\Delta G$is essentially pore-size independent, as discussed for classical nanopore blockade models[47].

In contrast, when the access resistance is appreciable (thin membranes or larger d), Eq. 12 predicts that ΔG acquires a clear dependence on the pore diameter: for fixed analyte size d_a, the relative volume excluded by the analyte decreases with increasing d, and the unchanged access term further reduces the fractional change in total resistance. This framework, which combines the Hall conductance with a volume-exclusion model for the analyte, is the same as that used in the quantitative analysis of dsDNA blockades in reference and provides a consistent basis for interpreting the pore-size dependence of blockade amplitudes in thin solid-state nanopores[59.]

---

[*] **A molecular blockade reflects ion exclusion and altered access resistance inside the nanopore sensing volume.**

2.5 Electric field in and around a nanopore

When a potential difference is applied across a nanopore of diameter d and membrane thickness l, the resulting electric field is not solely confined to the pore interior; instead, the potential extends into the electrolyte reservoirs on both sides of the membrane and decays radially away from the pore opening “mouth”. This behavior follows from the classical Maxwell–Hall analysis of current convergence into a circular aperture, which shows that the total voltage drop is shared between the pore (channel) resistance and the access (spreading) resistance in the reservoirs[48,49]. As a result, the reservoir potential near the pore exhibits an approximate $1/r$-type radial decay, where r denotes the distance from the centre of the pore opening ($r = 0$ at the mouth).

The electric field generated by the applied DC voltage ΔU is generally focused to the pore but will also be present outside. The potential will vary radially

$$\boxed{U(r) \approx \frac{d^2}{r\,(2\pi d + 8l)}\,\Delta U, r \gtrsim \frac{d}{2}} \qquad \text{(Eq.13)}$$

which makes explicit (i) the $\frac{1}{r}$ decay dictated by the access solution and (ii) the geometric factor $(2\pi d + 8l)$ that aggregates the spreading (access) and channel contributions in series. The numerical coefficients arise from the standard Hall treatment of a circular aperture (access) combined with a cylindrical pore (channel) and are widely used in solid-state nanopore analyses to approximate the near-field potential distribution[44].

Equation (13) assumes: (i) a cylindrical pore with circular orifice; (ii) Ohmic conduction (no significant rectification); (iii) negligible surface-charge and electro-osmotic effects (high-salt limit); and (iv) observation points outside the pore but close to the mouth in the region where hemispherical current spreading dominates[*]. This simplified form is particularly useful for analysing the event-frequencies and capture-radius at high voltages, where the strength of the reservoir field near the pore governs the transition from diffusion-dominated transport in the bulk to electrophoretic capture within a few micrometres of the

---

[*] **In barrier-free capture, event frequency scales with voltage and concentration; surfaces tune transport and fouling.**

orifice. In practice, the same geometric partitioning underlies expressions for capture radius and frequency - voltage relationships used in modern solid-state nanopore quantification.

2.6 Diffusion - controlled event frequency

When molecules that reach the pore mouth translocate immediately i.e., there is no additional free-energy or kinetic barrier after capture - the rate-limiting step is the diffusive supply of analyte from the bulk to the capture zone near the pore. In this diffusion-limited (or diffusion-controlled) regime, the maximal event frequency $f_0$follows directly from the Smoluchowski[60] capture flux into the electrically focused region surrounding the pore. Using the standard access + channel voltage partition (Hall/Maxwell framework), one obtains the linear frequency–voltage law[61–64]:

$$\boxed{f_0 \ = \ C_0 \, \mu \ \frac{2\,\Delta U}{d + 4l}} \Leftrightarrow \boxed{\frac{f_0}{C_0} \ = \ \mu \ \frac{2\,\Delta U}{d + 4l}} \qquad \text{(Eq.14)}$$

Here in the Eq 14, $C_0$is the bulk concentration (number density) of analyte (e.g., dsDNA), μ its electrophoretic mobility of the analyte, ΔU the applied bias, $d\ is$ the pore diameter, and l the membrane thickness; the denominator $(d + 4l)$ is the access plus channel geometric factor that describes how the applied voltage is partitioned between the pore and the surrounding electrolyte. Under diffusion-limited, barrier-free capture, the slope of f vs ΔU is therefore proportional to C.

A key prediction of Eq. (14) is that the event frequency is independent of the diffusion coefficient D: diffusion determines the supply to the capture zone, but once the field dominates (inside the capture radius) and the pore is not rate-limiting, the net rate is set by electrophoretic drift, i.e., by mobility μ rather than D. Consequently, $f_0$scales linearly with μ and ΔU, and inversely with the geometric factor $(d + 4l)$.

For double-stranded DNA[*], the effective electrophoretic mobility is nearly independent of contour length over typical nanopore buffer conditions (high-salt, room temperature), implying that f_0 does not vary strongly with DNA length as observed when comparing 2 kbp and 3 kbp dsDNA in the linear regime[58].

---

[*] **Capture can be diffusion limited when pore entry has no major barrier**

2.7 Surface functionalization and polymer brushes

Surface modification using polymer brushes has emerged as a highly versatile approach for tailoring the chemical and physical properties of interfaces[65–68]. By end-anchoring polymer chains to a solid substrate, one can precisely control surface wettability, chemical functionality, steric interactions, and biofouling resistance, thereby enabling significant advancements in materials science, nanotechnology, and biosensing applications.

In RPS, nanopore surfaces can be modified with polymer brushes to control analyte-surface interactions, reduce fouling, and tune electroosmotic flow. For example, grafting hydrophilic brushes inside nanopores can reduce adsorption of proteins or nanoparticles, ensuring more reproducible translocation events and clearer pulse signals. Stimuli-responsive brushes can further allow dynamic modulation of pore diameter or surface charge, enabling controlled gating or selective analyte passage.

Polymer brushes[69] are defined as thin polymer films in which individual polymer chains are tethered by one end to a solid interface at high grafting density which forces them to stretch away from the surface and adopt extended conformations. The most important characteristics of polymer brushes are the film thickness, as well as the chemical composition, molecular weight, dispersity and grafting density of the surface-tethered polymer chains.

Polymer brushes extend the random walk model of isolated chains to densely grafted systems on surfaces, where chain-chain interactions dominate, leading to stretched conformations and universal scaling behaviours. At low grafting densities, the polymer chains are sparsely distributed and adopt relaxed configurations, often referred to as the “mushroom” or “pancake” regime as shown in figure 7. In these regimes, the polymer coils do not interact significantly with neighbouring chains and remain largely unperturbed by steric forces. As the grafting density increases[*], steric repulsion between neighbouring chains forces the polymers to stretch away from the surface. In the high-density brush regime, which is defined as the limit where grafting density is sufficiently high that chains are forced into extended

---

[*] **Polymer brushes tune nanopore surface chemistry and molecular transport.**

conformations and chain - chain interactions dominate the structure – the polymers form a dense, nearly uniform layer[70,71]. Although the term "polymer brush" is used colloquially to describe all surface-tethered polymers, it properly applies only when the grafting density is high enough to produce this extended, interaction-dominated regime.

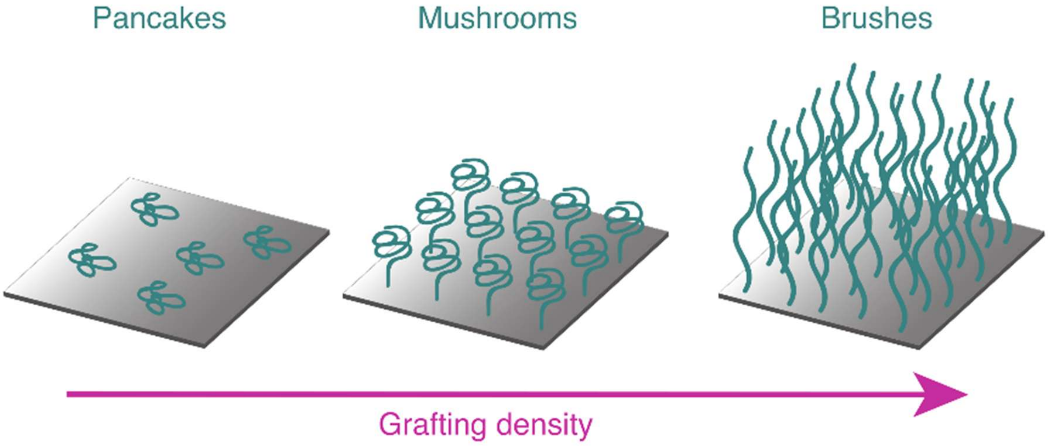

Figure 8 - Polymers based on grafting density. Reproduced from Ref. [72]

2.7.1 Synthesizing polymer brushes

Polymer brushes[*] can be synthesized using different strategies as shown in figure 8 namely 'grafting to' and 'grafting from' approaches. Each method has its advantages, and limitations. Although both the grafting to and grafting through techniques are experimentally straightforward, the grafting from method is often preferred because it typically yields significantly higher grafting densities and thicker brush layers[73].

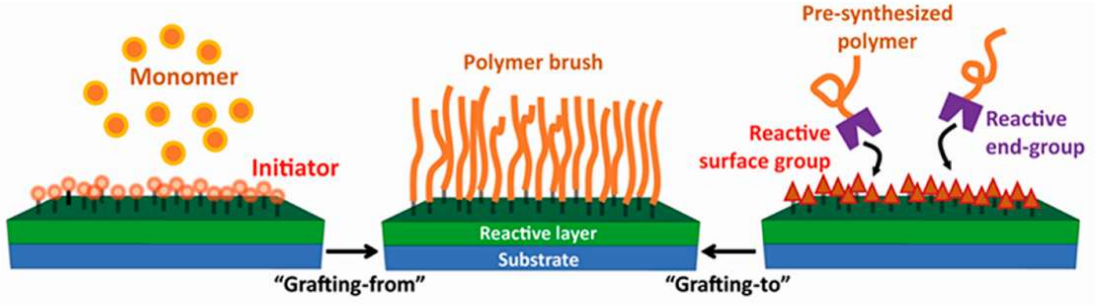

Figure 9 - Grafting polymer brushes. Reproduced from [74]

---

[*] **Polymer brushes can be synthesized by different methods like 'grafting to' or 'grafting from' methods.**

2.7.1.1 Grafting to approach

In the grafting to approach, pre synthesized polymers bearing reactive end functional groups such as amine, thiol, carboxyl, or silane moieties are chemically attached to complementary functional groups on the substrate surface. A key advantage of this method is that the polymer can be fully characterized prior to immobilization, enabling precise control over molar mass, dispersity, composition, and architecture. As a result, highly well-defined brushes can be obtained[75]. However, 'grafting to' is intrinsically self-limiting. As the brush layer grows, incoming polymer chains must diffuse through an increasingly dense layer of tethered molecules to reach the reactive surface. This steric barrier often referred to as an "excluded volume" effect restricts the achievable grafting density and limits the final brush thickness.

2.7.1.2 Grafting from approach

The grafting from approach relies on surface-initiated polymerization (SIP), where the substrate is first functionalized with initiator groups capable of triggering polymer chain growth directly from the surface. This strategy is considered a bottom-up method, as polymer chains are generated in situ at the interface. Because the tethered initiators are small molecules, they can be densely packed, thereby enabling much higher grafting densities compared to 'grafting to' method. Moreover, the brush thickness is directly related to the molecular weight of the growing chains, allowing precise control over film height by tuning the polymerization conditions. SIP is compatible with a wide range of polymerization mechanisms including surface-initiated atom transfer radical polymerization (SI-ATRP), surface reversible addition–fragmentation chain transfer polymerization (S-RAFT), surface-initiated nitroxide-mediated polymerization (SI-NMP), and surface-initiated photoiniferter-mediated polymerization (SI-PIMP), which makes grafting from one of the most widely used techniques for synthesizing dense polymer brushes[73,76].

Characterization of polymer brushes typically employs a range of analytical techniques, including ellipsometry for determining film thickness, atomic force microscopy (AFM) for assessing surface topography, X ray photoelectron spectroscopy (XPS) for probing chemical composition, and surface plasmon resonance (SPR) for monitoring brush growth and functionalization. In the present work, SPR is used as the primary method for brush characterization and the shift in plasmon angle can be fitted using Fresnel modelling to calculate the effective dry or hydrated brush thickness.

2.8 Surface Plasmon Resonance

Surface Plasmon Resonance (SPR) is a highly sensitive, label free optical technique that detects minute refractive index changes occurring within the surface region of a sensor because the method can resolve mass variations on the order of 0.1ng cm^{-2}. SPR[*] enables continuous monitoring of interfacial processes at nanometric length scales. Most SPR instruments employ flow cell configurations equipped with inlet and outlet channels, allowing both dry and liquid measurements and enabling real time monitoring under controlled flow conditions. Depending on instrument design, some systems can simultaneously determine the bulk refractive index of the medium above the sensor surface providing additional contextual information without requiring a separate reference channel.

SPR is based on exciting collective electron oscillations (surface plasmons) at a metal - dielectric interface and detecting how their resonance condition shifts when the refractive index near the surface changes. In a typical SPR biosensor, polarized light is directed through a prism onto a thin metal film (usually gold/palladium) at a specific angle. At one particular incidence angle (or wavelength), the in-plane momentum of the photons matches that of surface plasmons, so energy is transferred from the light to these plasmons, producing a sharp dip in the intensity of reflected light which is the SPR angle. This resonance angle is highly sensitive to the refractive index within the evanescent field (a few hundred nanometres) above the metal. When biomolecules bind to ligands immobilized on the gold surface, they increase the local refractive index, which shifts the SPR angle (or resonance wavelength). By monitoring this shift over time, SPR provides a label free measurement of mass accumulation at the surface, from which binding kinetics (association/dissociation rates), affinities, and concentrations can be quantified via sensorgrams[77].

---

[*] **SPR monitors interfacial mass and refractive-index changes without labels, enabling polymer brush characterization.**

2.8.1 Fresnel modelling for SPR data analysis

In SPR, the measured response typically the resonance angle θ_{SPR} or resonance wavelength arises from the interaction of incident light with a multilayer system consisting of the prism, metal film, any surface bound layers (such as polymer brushes), and the surrounding medium. Because each layer contributes differently to the optical response through its thickness and refractive index, quantitative interpretation of SPR data requires an optical model that describes how light propagates and reflects through stratified media. This analysis is commonly performed using Fresnel modelling.

Fresnel modelling* is based on the classical Fresnel equations, which describe the amplitude and phase of reflected and transmitted light at the interface between two materials with different refractive indices. For SPR, these equations are applied to a multilayer stack (e.g., prism / gold film / polymer brush / solution), using a transfer matrix to compute the overall reflectivity as a function of incident angle or wavelength. The model incorporates the complex refractive index of each layer, the thickness of each layer, the wavelength and polarization of the incident light and the boundary conditions imposed by Maxwell's equations.

By numerically solving the multilayer system, the model generates a theoretical reflectivity curve that can be compared point-by-point across a range of incident angles (or wavelengths) to the experimental data. The optical parameters (typically the refractive index and thickness of the surface-bound film) are adjusted iteratively until the calculated reflectivity curve matches the experimental reflectivity curve across the full angular (or wavelength) range, not just at a single resonance condition. This is more comprehensive than fitting to the resonance angle alone, because it uses information from the entire reflectivity profile. Because the penetration depth of the evanescent field is on the order of 100–200 nm, SPR combined with Fresnel modelling provides a highly sensitive, quantitative method for characterizing nanoscale polymer layers under fully solvated conditions. However, a fundamental challenge in both Fresnel and other optical models is the ambiguity between layer thickness and refractive index: multiple combinations

---

*** Fresnel modelling connects SPR reflectivity curves to polymer-layer thickness and refractive-index estimates.**

of these parameters can produce similar reflectivity curves, making it difficult to determine both quantities uniquely from optical data alone without additional constraints or independent information[78].

In summary, Fresnel modelling[*] serves as the quantitative optical framework that relates the full reflectivity curve to the physical properties of the interfacial layers. Without such modelling, the raw resonance angle alone cannot uniquely determine layer thickness or refractive index. The combination of precise optical measurements across a range of angles (or wavelengths) and rigorous multilayer modelling is therefore essential for quantitative characterization of polymer brushes using SPR.

---

[*] **Fresnel modelling serves as the quantitative optical framework that relates the full reflectivity curve to the physical properties of the interfacial layers.**

Chapter 3

Experimental

Overview

This chapter provides a comprehensive description of the experimental procedures employed for nanopore fabrication using the CDB technique, subsequent pore conditioning, polymer brush grafting, and polyethylene glycol (PEG) modification for molecular translocation studies. The operational methods for the Elements (EMCR) and Axopatch 200B amplifiers are also outlined, along with the cleaning and functionalization procedures used for gold-based SPR sensors.

3.1 CDB for nanopore fabrication

Nanopores were fabricated[*] through the CDB method, in which an intact silicon nitride membrane is immersed in an electrolyte solution and subjected to an electric field applied across Ag/AgCl electrodes. When the local electric field reaches a critical strength, a dielectric failure occurs that results in the formation of a nanometre-sized pore[42]. This pore can subsequently be enlarged and stabilized to achieve the desired final size using a controlled conditioning process. The SPARK E2 system (Northern Nanopore Instruments) was employed to automate this fabrication procedure, providing precise control over voltage ramping, breakdown detection, and conditioning steps.

3.1.1 Flow cell assembly and membrane wetting

Low-noise silicon nitride membranes (20 nm thickness, Norcada) were mounted within a two-piece fluidic flow cell integrated with silicone gaskets to ensure a leak-free assembly. To ensure complete membrane wetting, a 50:50 (v/v) mixture of isopropanol (IPA) and Milli-Q water was introduced gently into the flow cell using a 200 µL pipette, applying minimal pressure to avoid damaging the membrane. The flow cell was then flushed three to four times with 1 M KCl solution

---

[*] **Reliable nanopore fabrication starts with clean wetting, filtered electrolytes, and controlled voltage ramps.**

for electrical measurements and Ag/AgCl electrodes were inserted into the electrode caps and mounted onto the flow cell for electrical connection.

3.1.2 Buffer preparation

All electrolytes and buffers used for nanopore fabrication, conditioning, and translocation measurements were prepared with high-purity reagents. The solutions included 1 M KCl with or without TE buffer (10mM Tris, 1mM EDTA, pH 8; depending on experimental requirements), 3.6 M LiCl for conditioning, and a 50:50 (v/v) IPA:MilliQ water mixture for membrane wetting. Each solution was degassed to reduce bubble formation for 20 minutes prior to use and filtered through a 0.22 µm syringe filter (VWR or Cole Parmer) to remove particulates and prevent contamination during experiments.

3.1.3 Nanopore fabrication using SPARK E2

The prepared flow cell was inserted into the SPARK E2[*] system and connected to a computer running the Nanopore Fabrication software. For the standard 20 nm thick membranes, the fabrication protocol consisted of two voltage ramps: an initial rapid ramp to a starting bias of –5 V at a rate of 3 V min^{-1}, followed by a slower ramp toward a higher bias to induce dielectric breakdown, as illustrated by the applied voltage and current evolution in Figure 9. The starting bias was selected carefully to remain below the breakdown threshold specific to the membrane thickness, and the slower ramping stage increased the likelihood of capturing the exact onset of breakdown. Breakdown was identified automatically by a sudden surge in ionic current, detected through an adaptive algorithm that compares the median of the last 50 current samples against a user-defined threshold; once this threshold was surpassed, the instrument immediately terminated the voltage, confirming successful pore formation. Immediately after fabrication, the nanopore was characterized by recording a current–voltage curve in symmetric high-salt electrolyte to verify Ohmic behaviour and estimate the pore conductance, as shown in Figure 10. The nanopore diameter was then estimated

---

[*] **The SPARK E2 system automates pore formation and conditioning.**

from the measured conductance using the standard cylindrical pore model (Eq. 1), assuming Ohmic conduction in high-salt conditions.

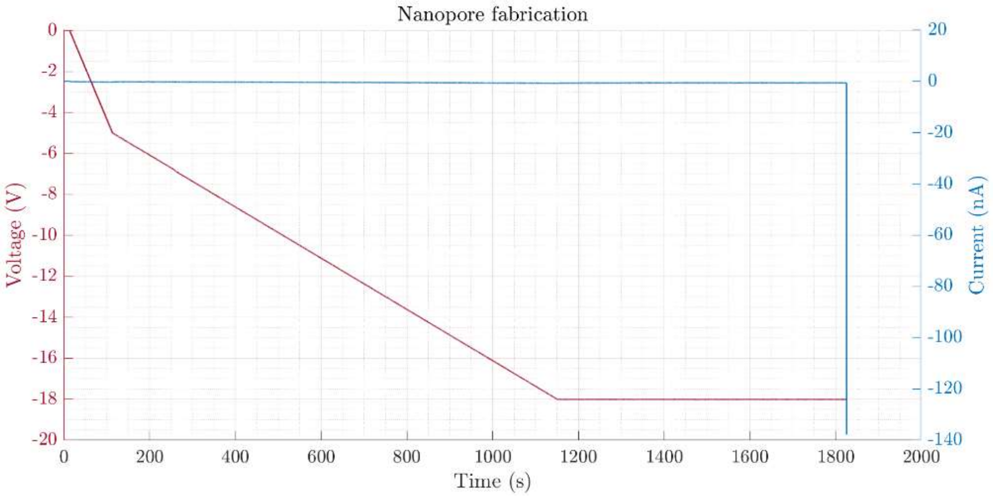

Figure 10 - Fabrication showing the applied voltage and the evolution of current during CDB

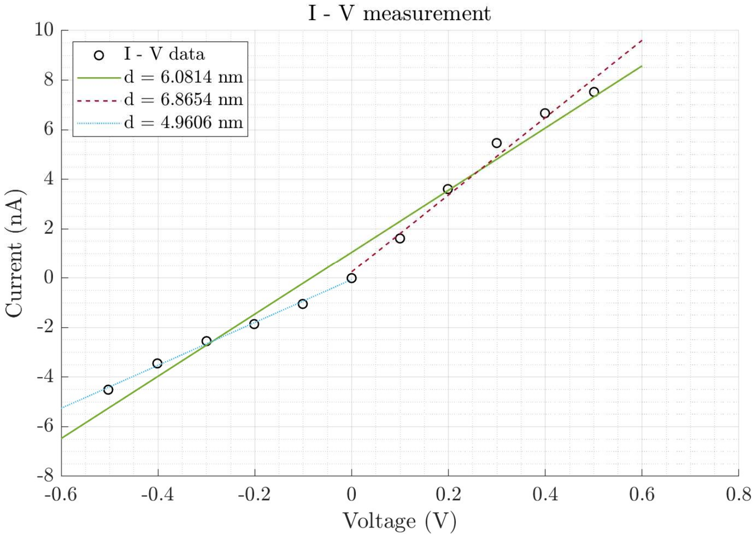

Figure 11 - Example of a current-voltage measurement recorded immediately after nanopore fabrication*

*** Conductance measurements verify pore formation, while voltage-pulse conditioning tunes the final pore size.**

3.1.4 Conditioning of nanopores

Following fabrication, nanopores smaller than the target diameter was enlarged through controlled electrical conditioning in 3.6 M LiCl solution using symmetrical voltage pulses ranging from +3 V to −3 V with a pulse width of four seconds. The ionic current was continuously monitored, and incremental increases in current indicated progressive pore widening.

Conditioning was manually terminated once the desired conductance value corresponding to the target pore size was achieved. The electrolyte was then replaced with 1 M KCl, and current–voltage (I–V) characteristics were recorded using the WinWCP software. Pore stability[*] was further verified by allowing the system to equilibrate for several minutes, followed by a repeat I–V measurement as in figure 11 to confirm consistent conductance and electrical stability over time.

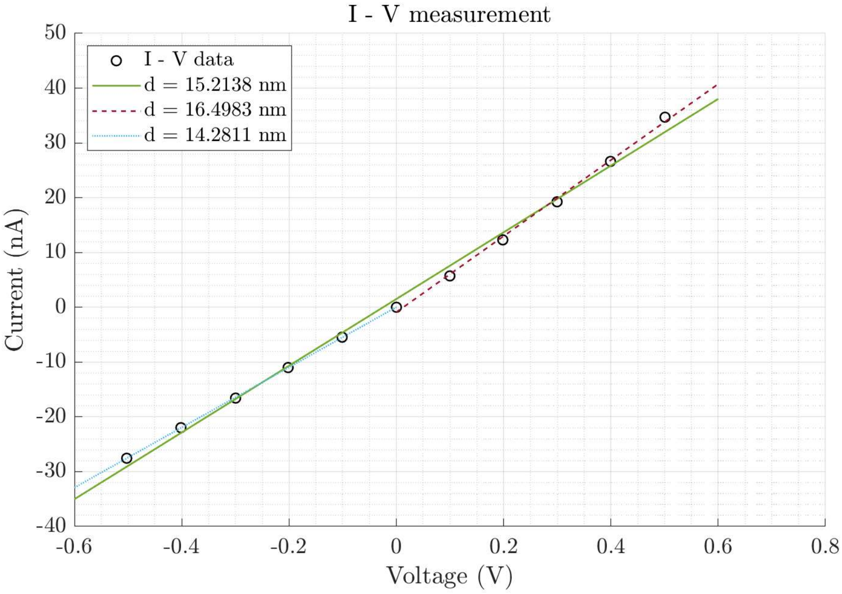

Figure 12 – Example of a current – voltage measurement after conditioning and stability verification of the same pore

---

[*] **Only stable, low-noise pores are carried forward for polymer grafting and molecular sensing experiments.**

3.2 Polymer brush grafting on nanopores

Surface functionalization of nanopores with polymer brushes was carried out to modify the pore surface chemistry, regulate molecular transport properties, and suppress nonspecific adsorption. PEG chains were grafted onto the nanopore surface following a laboratory protocol previously developed in the group[79] which shows a simple method for passivation or selective biofunctionalization of silica, without the need for polymerization reactions or vapor-phase deposition. This surface modification approach allows precise control over polymer chain density and thickness, thereby enabling systematic tuning of surface hydrophilicity and steric effects, while maintaining compatibility with delicate silicon nitride membranes.

3.2.2 Preparation of piranha - cleaned nanopore chips

The nanopore chips were cleaned using piranha solution to remove organic contaminants and activate the surface with hydroxyl groups. The cleaning solution consisted of a 3:1 (v/v) mixture of concentrated sulfuric acid (H_2SO_4) and hydrogen peroxide (H_2O_2). Safety Note: Piranha solution is highly corrosive and reacts violently with organic materials; therefore, all procedures were performed inside a fume hood under strict safety precautions. The Norcada silicon nitride chips were immersed in freshly prepared piranha solution for 20 minutes. Following treatment, the chips were thoroughly rinsed multiple times with Milli-Q water to remove any residual oxidants. The cleaned membranes were used immediately for nanopore fabrication followed by silanization or stored temporarily in Milli-Q water to preserve the activated surface. This process generated a hydroxyl-rich, hydrophilic silicon nitride surface that is highly suitable for subsequent silane-based coupling reactions.

3.2.3 Silanization and PEG grafting

Following pore fabrication, the SiN_x surfaces were chemically functionalized* via silanization using reagents including 3 aminopropylsilatrane (APS),

---

* **PEG modification passivates pore surfaces and reduces nonspecific biomolecular adsorption.**

sulfosuccinimidyl 4-(N-maleimidomethyl) cyclohexane-1-carboxylate (SMCC), and PEG, following the established laboratory protocol. The ethanol rinsed chips were first immersed in APS solution to introduce amine groups, allowing subsequent coupling to the bifunctional crosslinker SMCC. The final PEG grafting step was achieved by incubating the silanized chips in PEG solution for two hours at room temperature prior to electrical measurements. This multi-step process resulted in the formation of a covalently bonded PEG layer with controlled polymer density and thickness on the nanopore surface.

3.2.4 Post - grafting characterization

Successful polymer brush grafting was verified through nanopore characterization based on current–voltage (I–V) analysis. A distinct reduction in ionic conductance after grafting indicated the presence of the PEG layer on the nanopore surface, consistent with the reduced effective pore diameter due to the grafted polymer coating. The I-V curves remained ohmic and stable, confirming that the neutral PEG brush did not introduce significant charge or ion current rectification. Only nanopores exhibiting stable I–V characteristics, low noise levels, and no leakage currents were used for subsequent molecular translocation experiments.

3.3 Preparation of DNA, and protein analytes

DNA double strands of defined lengths (2 kbp and 3 kbp) and proteins were reconstituted according to the manufacturer's instructions and stored at -20 °C unless otherwise specified. For experiments, samples were diluted in filtered analysis buffer, typically containing 1 M KCl with Tris EDTA (TE) buffer, to obtain working concentrations in the range of 10 - 100 nM. Protein analytes such as ferritin, avidin, β galactosidase, tau protein etc were initially dissolved in the respective recommended buffers (e.g., PBS or Milli Q water) and further diluted to 1 - 100 nM in the appropriate electrolyte immediately before use. The prepared analyte solutions were stored at 4 °C and used within a few days to avoid degradation or aggregation*.

*** Functionalized nanopores must remain electrically stable after surface modification whereas DNA and proteins provide model analytes for sensing studies.**

3.4 Elements Nanopore Reader (10 MHz operation)

3.4.1 System overview

The Nanopore Reader 10 MHz (Elements srl) is a high-bandwidth, single-channel current amplifier specifically designed for solid-state nanopore applications. It is described as the world's first single channel 10 MHz current amplifier for nanopore applications, enabling the detection of extremely fast translocation events that are inaccessible to conventional low-bandwidth electrophysiology amplifiers. The instrument integrates a low noise transimpedance amplifier with a dedicated flow cell interface, high-speed digitization, and real time control software in a compact benchtop platform.

The system provides a measurement bandwidth up to 10 MHz with a typical dynamic range of approximately ±100 nA and sampling rates up to 40 MS/s (mega samples per second) (i.e., 40 million current measurements per second), allowing accurate recording of sub microsecond current blockades arising from nanoparticle or biomolecule passage (translocation) through solid-state nanopores. The amplifier and digitizer are optimized for low input noise over a wide frequency range, which is essential for resolving small blockade events at high temporal resolution. The Nanopore Reader 10 MHz is therefore particularly suited for measurements on solid-state nanopores, where short dwell times and high event rates demand both wide bandwidth and stable baseline performance[*].

3.4.2 Flow cell installation and baseline recording

Before analyte introduction, the nanopore chip was mounted in the Elements flow cell chamber and filled with the desired electrolyte solution. A holding potential in the range of −100 mV to −300 mV, depending on pore size, was applied to establish a baseline ionic current. Baseline measurements were recorded for 60–120 seconds to ensure a stable open-pore current, minimal 1/f noise, and absence of current drift or leakage. Nanopores exhibiting excessive noise, unstable current baselines, or spontaneous fluctuations were discarded prior to analyte testing.

---

[*] **High-bandwidth electrical recording resolves fast blockades produced by molecules in solid-state nanopores.**

3.4.3 Translocation Experiments

For molecular translocation measurements, the analyte solution was added to the cis side of the flow cell unless otherwise specified. A constant bias voltage, typically –200 mV for DNA capture and transport, was applied to drive the translocation process. Data were acquired at a raw sampling rate of 500 kHz and digitally filtered to 100 kHz using the built-in amplifier filter. Each experimental run lasted 10–30 minutes, depending on event frequency and stability. All raw current traces were saved for offline analysis using MATLAB. Translocation events were characterized by their fractional current blockade depth ($\Delta I/I_0$) and dwell time (τ).

3.4.4 Cleaning and Reuse of Nanopores that are clogged

Between experiments, nanopores were thoroughly rinsed three to five times with the supporting electrolyte to remove any residual analyte. A mild voltage sweep was applied to check for potential clogging or excessive noise. If pore blockage could not be resolved through flushing, the chip was discarded, as PEG-grafted pores could not be subjected to chemical cleaning without damaging the polymer layer.

3.5 Surface preparation and functionalization of SPR chips

SPR experiments were conducted on gold-coated sensor chips that required exceptionally clean, oxide-free surfaces to ensure reliable polymer brush grafting and biomolecule immobilization. Both piranha treatment and RCA-1[*] (TL-1) cleaning were employed as surface preparation methods.

Piranha cleaning was used for robust gold SPR chips that could withstand harsh oxidative chemistry. SPR gold chips were immersed in the piranha solution for 20 mins to remove organic contaminants and expose a hydrophilic gold surface, which is suitable for subsequent thiol-based self-assembly. However, piranha treatment is too aggressive for nanopore samples with exposed chromium adhesion layers, so RCA-1 cleaning was used as a milder alternative for those substrates. The RCA-1 solution consisted of five parts Milli-Q water, one part ammonium hydroxide

---

[*] **RCA -1 cleaning is also known as TL-1 cleaning**

(NH_4OH), and one part hydrogen peroxide, and was heated to 75 - 80 °C prior to use. SPR chips were immersed in this solution for 20 minutes, then rinsed thoroughly with Milli-Q water and dried under a nitrogen stream. This procedure efficiently removed organic films and particulate contamination while avoiding damage to exposed metal layers beneath the gold coating. For preparation of thermoresponsive polymer brushes, SI ARGET-ATRP of poly(N - isopropylacrylamide) (P-NIPAM) was performed from initiator-functionalized SPR chip surfaces to enable "grafting from" growth of PNIPAM brushes. Gold-coated chips were first cleaned and then immersed in an ethanolic solution (1 mM) of the thiol ATRP initiator 11 mercaptoundecyl 2 bromo 2 methylpropanoate for 12–24 hours at room temperature. After self-assembly of the initiator monolayer via Au - S chemisorption, the chips were removed and thoroughly rinsed with ethanol to remove loosely bound species. The resulting initiator-functionalized gold surface served as the starting platform for subsequent SI ARGET ATRP polymerization of NIPAM to form P-NIPAM brushes.

NIPAM (MW - 113.16 g mol^{-1}) was polymerized from surface-bound ATRP initiators using a catalyst system comprising $CuBr_2$ and N,N,N',N'',N'' pentamethyldiethylenetriamine (PMDETA), with ascorbic acid serving as th reducing agent in a 70:30 (v/v) Milli-Q water/methanol solvent mixture. The monomer solution was first degassed under nitrogen for 20 minutes to remove dissolved oxygen, after which the initiator-modified chips were introduced into the reaction vial. Polymerization was initiated by injection of ascorbic acid and allowed to proceed for 30 - 120 minutes, depending on the targeted brush thickness. The reaction was quenched by exposure to air, and the chips were subsequently removed, thoroughly rinsed with ethanol, and dried under nitrogen*.

3.5.1 SPR measurements of brush growth

SPR measurements of polymer brush growth were performed using a BioNavis Navi 220A instrument. SPR resonance curves were recorded after polymerization, and the increase in optical thickness associated with brush formation was quantified from the shift in resonance angle extracted from the recorded spectra. The resonance curves were analyzed using SPRpy, a Python-based SPR analysis software

---

* **Exceptionally clean surfaces are used for polymer brush grafting**

developed in-house, which implements Fresnel modelling for the SPR data. Brush thickness and refractive index were extracted by fitting a multilayer optical model to the experimental SPR response. The multilayer model incorporated appropriate optical constants for the glass substrate, chromium adhesion layer, gold film, polymer layer, and buffer solution.

Growth of the polymer brush produced a progressive increase in the SPR resonance angle and a corresponding increase in the calculated optical thickness of the surface-bound layer, confirming successful ATRP polymerization on the gold surface. The dry brush thickness was determined from the fitted refractive index and optical thickness of the polymer layer. To estimate the swollen brush height under solution conditions, the refractive index of the hydrated polymer layer was compared with tabulated values for fully hydrated PEG, and the thickness was calculated assuming a linear relationship between swelling and the change in local refractive index.

Chapter 4

Results and Discussion

Published Results

4.1 Paper I – Analyte quantification

This chapter summarizes the first[*] research article included in this licentiate thesis, 'Solid-State Nanopore Sensors: Analyte Quantification by Event Frequency Analysis at High Voltages', published in ACS Analytical Chemistry in February 2025. My contribution to this paper was mainly in the experimental nanopore measurements and the data-analysis workflow. I recorded ionic-current traces, including high-voltage measurements, and contributed to MATLAB-based event detection and extraction of event frequency, blockade amplitude and dwell time. This contribution was most directly connected to testing the high-voltage event-counting strategy and the concentration-readout method.

Background and motivation

The relationship between event frequency (i.e; how often translocation events occur) and applied voltage has been underexplored, despite being central for quantification and for understanding electrophoretic capture and transport physics. Previous studies often operated at relatively low voltages to avoid baseline instabilities, limiting the analysis to a narrow voltage range and preventing systematic characterization of the event frequency – voltage dependence.

Theoretical studies indicate that for a barrier free, diffusion limited pore, event frequency should scale linearly with voltage, whereas for pores

---

[*] **Paper I turns nanopore event frequency into a direct route for analyte concentration measurement.**

presenting an entry barrier (e.g., narrow pores requiring specific conformations), event frequency should exhibit exponential voltage dependence. Such exponential behavior has been reported for DNA threading through pores only a few nanometers wide and in biological nanopores but had not been systematically contrasted with larger solid-state pores across a broad voltage range. This gap motivates a detailed combined experimental - theoretical study of event frequency versus voltage, directly linked to concentration.

Scientific overview

The paper presents a calibration-free approach for determining analyte concentration in solid-state nanopore experiments. In many previous nanopore studies, quantification relied on external calibration, where the nanopore signal (typically blockade amplitude or dwell time) is compared against measurements of reference analyte with known concentration[80]. Instead of this approach, the method presented here extracts quantitative concentration information directly from the relationship between event frequency and applied voltage, without requiring any external reference species or calibration standards. The work demonstrates that this voltage - event frequency dependence provides a reliable means of concentration measurement, expanding the analytical capabilities of nanopore sensors.

Traditionally, nanopore research has largely focused on characterizing molecular properties such as size, shape, and charge, as well as the influence of pore surface chemistry. In contrast, the direct relationship between analyte concentration and nanopore signal output has been relatively unexplored. This study* represents the first systematic demonstration of concentration quantification based solely on event frequency behavior in solid-state nanopores.

---

* **Pore size is a key design parameter for frequency-based quantification.**

Purpose and research questions

The main purpose was to systematically investigate how event frequency depends on applied voltage in solid-state nanopores and to exploit this dependence to extract analyte concentration without external calibration. The paper also aims to understand under which conditions the event frequency - voltage relation is linear (diffusion-limited, barrier-free transport) versus exponential (barrier-limited), and how pore size, voltage, and transport parameters control this behavior.

The paper addresses three key questions:

1. Can event frequency-voltage curves be used directly to determine analyte concentration in a robust, calibration-free manner?
2. How do high voltages (up to 1 V) and resulting baseline instabilities affect reliable event counting, and can this be corrected algorithmically?
3. Does event frequency depend on electrophoretic mobility or diffusivity of the analyte, and how does this compare with theoretical expectations for diffusion-limited capture?

Methods

The study uses solid-state nanopores with systematically varied diameters, spanning above and below approximately 10 nm, to probe regimes of predominantly free translocation versus docking-dominated behavior. Double-stranded DNA (dsDNA) is selected as a model analyte, and two different DNA lengths are used to test how molecular length (which affects both diffusion coefficient and electrophoretic mobility) and the parameters (diffusivity and mobility) influences event frequency. The experiments are performed over a wide range of applied voltages, up to 1 V, specifically to enable analysis of the event frequency–voltage relationship across a large dynamic voltage range.

The core observable is the event frequency *f*, extracted from ionic current time traces, together with event amplitude ΔI and dwell time Δt to confirm the nature of the events (translocation vs docking). The data is recorded under conditions where analyte concentration is known, enabling direct comparison between measured frequency - voltage curves and theoretical predictions for diffusion-limited capture.

Signal processing and high-voltage data handling

A central technical contribution is the development of signal processing algorithms based on Fast Fourier Transform (FFT)[*] that allow accurate event counting at high voltages where baseline instabilities are significant.

One major achievement in this work is the development of an advanced data analysis framework capable of handling nanopore recordings at voltages up to 1 V - more than three times higher than those typically used. High voltage operation traditionally introduces substantial baseline instability and elevated noise, making event detection unreliable with existing commercial tools. By implementing FFT-based filtering together with an iterative, adaptive event counting approach, one could successfully stabilize the baseline and enable accurate detection of translocation events even in highly unstable current traces. This represents an essential breakthrough for expanding the usable voltage range of solid state nanopores and extracting meaningful information from otherwise inaccessible data.

An illustrative example is provided in Figure 12, showing a current trace recorded at 1V where significant baseline instability is present. After applying the FFT-based high pass filter at 100 Hz, the baseline variations are effectively removed, revealing a clean and stable trace suitable for analysis.

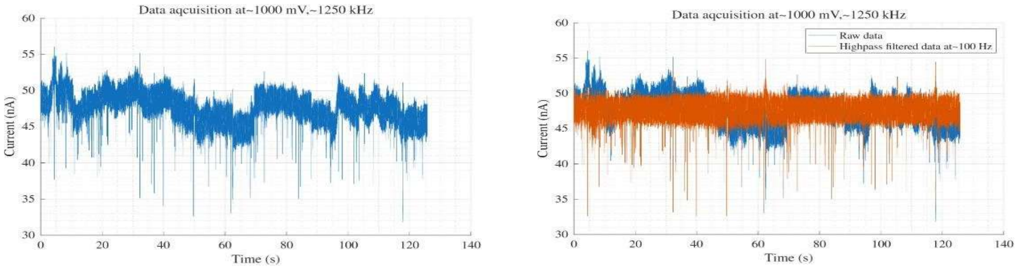

Figure 13 - Current trace recorded at 1V before and after correcting the baseline instability

---

[*] **FFT-based filtering enables event counting despite unstable high-voltage baselines.**

Results

For nanopores with diameters ≥ 10 nm, we find that the event frequency exhibits a clear linear dependence on the applied voltage over the investigated range, in agreement with diffusion limited capture into a barrier free pore. This linear scaling forms the basis of our quantification strategy, as the slope of the event frequency - voltage relation is directly proportional to the analyte concentration. In contrast, for smaller pores* the behavior changes qualitatively: the majority of events correspond to docking rather than full translocation, the linear frequency - voltage dependence is lost, and the response becomes characteristic of barrier limited entry, demonstrating that pore size determines the dominant event type and the appropriate theoretical framework and thus constitutes a critical design parameter for quantitative, frequency based nanopore sensing.

The dsDNA molecules are much longer than the pore dimensions, so they translocate by threading. The 2 kbp and 3 kbp dsDNA molecules have contour lengths much larger than the pore diameter and membrane thickness, so translocation requires threading of a polymer coil into the pore. The solutions are dilute, however, at the dilute concentrations used here they are not expected to be in an entangled bulk regime where classical reptation is the main transport mechanism, so the comparison should not be interpreted in terms of bulk reptation of entangled DNA chains. Instead, the relevant point for the frequency analysis is that the electrophoretic mobility of dsDNA is nearly length-independent under these conditions, whereas the diffusion coefficient changes with length. By comparing two double-stranded DNA lengths, we tested the predicted dependence of event frequency on electrophoretic mobility and diffusivity under diffusion-limited conditions. Electrophoretic mobility is independent of DNA length in our experiments, whereas diffusivity decreases with increasing DNA length. Accordingly, we observed no significant difference in event frequency between the two DNA analytes, consistent with the theoretical prediction that frequency depends on mobility

---

[*] **Small pores shift toward docking-dominated or barrier-limited behaviour.**

(which is similar for both lengths) and is independent of diffusivity under diffusion-limited conditions. These results support our theoretical model and confirm that mobility is the relevant transport parameter for comparing species in this regime.

Building on this insight, we established a calibration-free method to determine analyte concentration from event frequency - voltage data, in which translocation events are recorded at multiple voltages, the slope of the linear frequency – voltage relation is extracted, and this slope* is used to calculate concentrations without external calibration species or reference standards. When averaging approximately four experiments, the method yields concentration errors of about 10%, which is high accuracy for a label-free single-molecule technique, while single experiment estimates remain practically useful with errors below roughly 30%. In addition to frequency, we analyze how event amplitude and dwell time behave at high voltages: the amplitude increases linearly with voltage, indicating a constant conductance change per translocation and confirming that the pore constriction geometry remains stable over the entire voltage range studied, whereas dwell time decreases with increasing voltage, reflecting stronger electrophoretic forces that accelerate DNA and shorten translocation durations. The fact that we can still detect and quantify these short, high field events underlines the importance of our FFT-based signal processing framework, which enables robust event counting upto 1V despite increased baseline instability and noise.

---

* **The slope of frequency versus voltage can be used to calculate concentration.**

4.2 Paper II – Electric field effects

This part of the chapter summarizes[*] the second research article included in this licentiate thesis, 'The Electric Field in Solid State Nanopores Causes Dissociation of Strong Biomolecular Interactions', published in ACS Nano Letters in May 2025. My primary contributions to the study involved performing SPR measurements and the subsequent data analysis of the SPR data using SPRpy analysis software.

Background and motivation

Solid-state nanopores are widely used for label free electrical detection, often in schemes where a receptor–ligand pair is used for affinity-based capture, or where biomolecules are trapped and held inside or near the pore. Because the membrane thickness is typically on the tens of nanometer scale, even modest voltages of a few hundred millivolts generate axial fields around 10^7 V/m, which are 2–3 orders of magnitude stronger than in gel or capillary electrophoresis[85]. In other electrophoretic contexts, such fields have already been suggested to denature proteins[86], and several nanopore studies have hinted at structural changes during translocation[87,88]. However, the explicit influence of such fields on binding interactions in terms of lifetimes of receptor - ligand complexes have rarely been addressed. Prior work mainly explored how applied voltage affects residence times for relatively weak or artificial interactions, for example histidine - NTA binding on metal-coated[89], conical pores, which are not directly representative of typical bioanalytical pores or strong biological interactions. This paper addresses that gap by focusing on a strong, well characterized biological interaction on conventional silicon nitride nanopores.

Scientific overview

This paper demonstrates that the intense electric field inside solid-state nanopores can actively disrupt strong biomolecular interactions, specifically

---

[*] **Paper II asks whether the nanopore electric field is a passive readout or an active perturbation.**

biotin – avidin bond, and therefore the sensing mechanism itself can perturb the molecules being measured. This has direct relevance for any work using nanopores for affinity based sensing or trapping, because it shows that the field can alter binding equilibria and kinetics by orders of magnitude compared to bulk conditions. In short, the paper provides the answer to the question 'can nanopore-based electrical sensing be considered non-perturbative for biomolecular interactions, or does the field fundamentally alter the systems being tested?'

Purpose and research questions

The main purpose is to determine whether the very strong electric field inside thin solid-state nanopores (on the order of 10^7 V/m) affects biomolecular interactions, and if so, to what extent and through which physical forces. For this study, we choose the biotin - avidin interaction[*], often regarded as the strongest noncovalent protein - ligand bond in biology, as a model system.

<u>The paper addresses three key questions:</u>

1. Can the nanopore electric field dissociate biotin–avidin complexes that would otherwise be essentially permanent on experimental time scales?
2. What are the relative roles of electrophoretic and electroosmotic forces in this dissociation process?
3. How do multivalent, streptavidin-coated nanoparticles behave under the same conditions, and does increased avidity protect against field-induced dissociation?

Results

The experiments show that avidin bound to biotinylated nanopores is essentially stable for hours at zero bias, but application of a DC voltage (visible already around 200 mV) causes a gradual conductance recovery that reflects rapid, field induced dissociation of the biotin–avidin complex. The effective bond lifetime is shortened by at least four orders of magnitude when voltage is

---

[*] **The biotin-avidin pair serves as a model for strong noncovalent binding.**

applied. Force analysis indicates that electrophoretic forces on the positively charged avidin protein dominate over electroosmotic drag and are strong enough to make bond breaking thermodynamically favourable, thereby accelerating dissociation in a voltage - dependent manner. This is consistent with the stochastic, voltage-dependent[*] release we observe.

For streptavidin-coated nanoparticles, multivalent biotin - streptavidin binding produces large, step-like conductance blockades. Even at 1 V for 30 min, no net release of the nanoparticle occurs, although chronoamperometry and simulations reveal lateral motion driven by repeated breaking and reforming of individual bonds. Overall, the results demonstrate that the nanopore electric field actively perturbs and can reorganize even very strong protein - ligand complexes, implying that kinetic and affinity parameters extracted from nanopore measurements may diverge from bulk values unless such field effects are explicitly accounted for in assay design and interpretation.

SPR measurements were used to determine the stoichiometry and surface coverage of the biotin - avidin complex under field-free conditions. After avidin injection onto a biotinylated surface, the SPR signal reached a stable plateau. Subsequent rinsing with buffer over timescales comparable to the nanopore experiments produced negligible signal decrease, confirming that spontaneous dissociation is extremely slow and effectively irreversible on the experimental timescale. In contrast, nanopore measurements show pronounced conductance recovery within minutes when a few hundred millivolts are applied, corresponding to at least a four order of magnitude reduction in effective bond lifetime. This dramatic difference - the absence of significant SPR signal loss without applied field and the rapid, voltage - dependent release in nanopores - demonstrates that the electric field, primarily through electrophoretic forcing on the positively charged avidin, is directly responsible for the accelerated dissociation.

---

[*] **The biotin-avidin system reveals that nanopore bias can shorten strong binding lifetimes by orders of magnitude.**

4.3 Unpublished results

Functional Nanostructures with Thermoresponsive PNIPAM Polymer Brushes

This part of the thesis explores two separate projects on thermoresponsive PNIPAM-grafted nanostructures as soft, switchable gates for both biomolecules and ions. In the first study, PNIPAM-modified gold and palladium nanowells are used to trap enzymes enabling localized fluorescence readout through a small fluorogenic substrate. In the second study, PNIPAM brushes are employed to see how the ionic conductance is modulated through a nanopore or nanopore arrays across different temperatures.

4.3.1Enzyme Confinement and Fluorescence Detection

Background and motivation

This study explores PNIPAM-grafted nanowells as thermoresponsive nanochambers for enzyme confinement and optical readout. PNIPAM undergoes a reversible coil - globule transition near its LCST (≈ 32 °C): below the LCST the brushes are hydrated and extended, while above they collapse into compact, more hydrophobic layers[90]. When grafted around nanowell openings, PNIPAM can thus act as a temperature-controlled gate that regulates access of large biomolecules while allowing small substrates and ions to pass. Previous work[93] has demonstrated that thermoresponsive polymer brushes can be used to trap and release biomolecules such as proteins and enzymes in nanoscale chambers while retaining enzymatic activity. However, most such systems have focused on relatively large cavities and ensemble behaviour. The present study aims to bring this concept toward the single molecule regime by using PNIPAM grafted nanowells with sub 100 nm diameters for enzyme confinement and readout by fluorescence microscopy.

Scientific overview

Gold and palladium nanostructures[*] (80–120 nm in diameter) are functionalized with PNIPAM brushes to create confined reaction volumes for β-galactosidase (β-gal). The enzyme is loaded when PNIPAM is collapsed at elevated temperature and then retained beneath the gate when the brush is rehydrated and extended below the LCST. Catalytic activity is probed with the fluorogenic substrate FDG, which can diffuse through the hydrated PNIPAM[†] layer and generates localized fluorescein fluorescence upon enzymatic cleavage. The central question is whether this architecture can confine catalytically active enzyme populations and, ultimately, approach single-enzyme occupancy.

Purpose and research questions

This work aims to demonstrate gated enzyme confinement in PNIPAM-modified nanostructures and to develop an optical readout that selectively reports on confined enzymes. The specific questions are:

1. Do PNIPAM-grafted nanostructures permit diffusion of the small fluorogenic substrate (FDG) to confined β-galactosidase, and can this configuration generate localized, time-dependent fluorescence signals from enzymatic turnover?

2. Under which physicochemical conditions (temperature, pH, and polymer conformation) do the PNIPAM brushes effectively suppress non-specific interactions between β-galactosidase and the surrounding surface walls?

3. How can the bulk enzyme concentration and loading protocol be tuned so that PNIPAM-gated nanowells approach single-enzyme confinement, rather than multi-enzyme occupancy, in individual cavities.

---

[*] **Gold and palladium nanowells with PNIPAM brushes provide confined environments for enzyme localization.**

Methods

Nanostructures and polymer brushes

Gold and palladium[81] nanostructures (nanowells) with nanoscale cavities were fabricated for molecular confinement experiments based on previously developed fabrication methods[46,78,82]. The nanostructures were produced on a SiO_2 substrate with chromium adhesion layer, followed by a 30 nm layer of either gold or palladium. Both gold and palladium were selected as substrate materials for the nanowell structures due to their compatibility with thiol based self-assembled monolayer (SAM) formation. Gold is extremely noble and highly resistant to oxidation; even when surface oxides form, they readily decompose to metallic gold, resulting in excellent SAM formation quality with minimal interference.

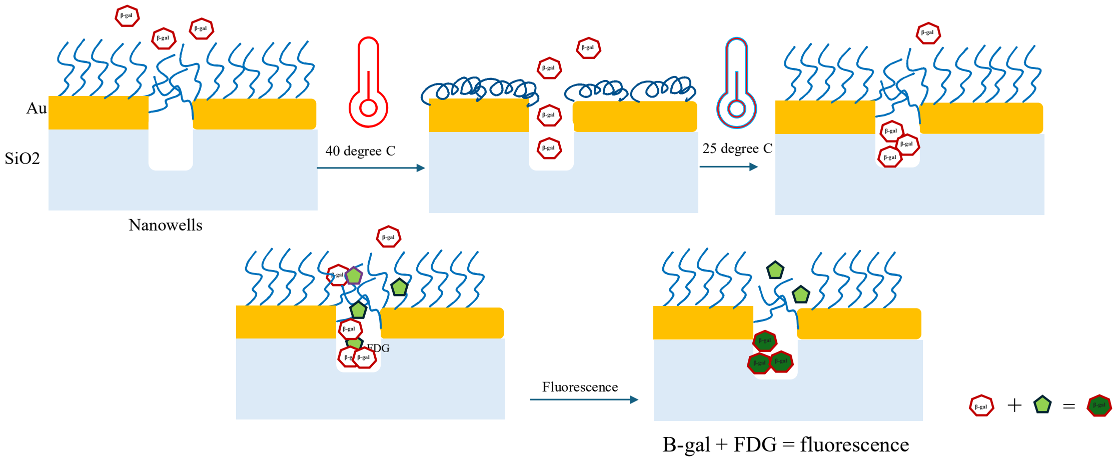

Figure 14 - Schematic of enzyme confinement in nanostructures

Palladium, in contrast, forms a stable palladium oxide (PdO) layer that significantly hinders thiol binding. For palladium nanostructures, a surface reduction step was therefore required prior to SAM formation to ensure uniform polymer brush grafting. Once the oxide layer was reduced, palladium supported thiol chemistry like gold, enabling PNIPAM[*] brush grafting into the palladium nanostructures through the same surface functionalization strategy. These structures were grafted with PNIPAM polymer brushes via ARGET ATRP[83,84]

---

[*] **The thermoresponsive switching of PNIPAM is reversible and repeatable over many cycles.**

(Activators Regenerated by Electron Transfer Atom Transfer Radical Polymerization), or the SARA (Supplemental Activators and Reducing Agents) method using a copper plate was employed, with a solvent mixture of 70% H_2O and 30% methanol, 11 mM $CuBr_2$, 40 mM Me_6Tren ligand, and 0.5 M NIPAM monomer. A 75 µm thick silicon elastomer gasket was used to contain the reaction mixture on the nanostructure surface. The SARA approach was not reliable to produce reproducible brushes, so mainly ARGET ATRP method was employed. The resulting PNIPAM brushes exhibited dry thicknesses of approximately 54–55 nm forming thermoresponsive soft barriers on the nanowell rims[*]. The proposed enzyme confinement mechanism is illustrated schematically in Figure 13.

The enzyme β-galactosidase (β-gal) was introduced as a model biomolecule to explore enzyme confinement and catalytic activity under reversible polymer gating. The enzyme β-gal from *Aspergillus oryzae* was chosen as the model biomolecule for confinement studies. β-gal is a large enzyme (molecular weight ~465 kDa, hydrodynamic diameter ~10–12 nm) that catalyzes the hydrolysis of β-galactosides[85]. The *A. oryzae* variant exhibits distinct biophysical properties compared to the more commonly used bacterial (*E. coli*) β-gal: its hydrophobic core contributes to structural stability under acidic and thermal conditions, making it suitable for industrial applications such as lactose hydrolysis[86]. Importantly, the *A. oryzae* enzyme is amphipathic to hydrophilic in character and does not rely on hydrophobic interactions for quaternary structure stabilization, unlike the *E. coli* enzyme which is more hydrophobic and requires such interactions for stability. This hydrophilic character makes the *A. oryzae* β-gal particularly suitable for surface immobilization and confinement experiments in aqueous environments[87].

Enzyme, loading protocol, and pH step

1. **Loading:** The sample is heated to ~60 °C (above the PNIPAM LCST and near the enzyme's optimal activity temperature) at pH 6. Under these conditions PNIPAM is collapsed and the nanowell entrances are open; β-gal can diffuse into the cavities and weakly adhere to interior surfaces.

---

[*] **Temperature cycling uses collapsed PNIPAM for loading and extended PNIPAM for enzyme retention.**

2. **Gating:** The temperature is then lowered below the LCST so that PNIPAM rehydrates and extends, covering the well openings and forming a soft barrier that suppresses enzyme escape while remaining permeable to small molecules.
3. **Desorption of non-confined enzyme:** After gating, the pH is raised to 8 to reduce β-gal adsorption on exposed SiO_2 and desorb enzymes that are trapped inside the cavity.

Fluorescence readout

FDG is added after the gating and desorption steps. As a small (~376 Da) molecule, FDG[*] can diffuse through the hydrated PNIPAM layer to the confined β-gal. Enzymatic cleavage releases fluorescein, producing localized fluorescence within nanowell regions. Fluorescence microscopy is used to monitor the emergence and growth of bright spots in the nanostructured areas.

Expected results and main findings

Fluorescence microscopy is expected to reveal bright, localized spots in the nanowell regions after FDG addition, with spot intensities increasing over time in a manner consistent with ongoing enzymatic turnover by confined β-galactosidase. With optimized PdO reduction and PNIPAM grafting, both gold and palladium nanowells should show similar confinement behavior, indicating that each metal supports effective brush formation and enzyme retention. At the same time, the anticipated fluorescence intensity levels suggest that most emitting regions will correspond to small clusters or populations of enzymes per well, rather than uniquely single molecules. Overall, the PNIPAM-grafted nanowells are therefore expected to provide gated confinement of catalytically active enzyme populations - demonstrating that enzymes can be loaded in the collapsed state, retained in the extended state, and probed via a small fluorogenic substrate - while also indicating that true single-enzyme confinement will require further tuning of enzyme concentrations, ideally 1uM concentration, to shift from multi-enzyme occupancy toward one enzyme per cavity.

---

[*] **FDG turnover produces localized fluorescence, showing that confined beta-galactosidase remains catalytically active.**

4.3.2 Ionic conductance through PNIPAM-modified nanostructures

Background and motivation

The ionic conductance measurements were performed on PNIPAM-modified nanopores to explore how polymer brush conformation influences ion transport. Thermoresponsive PNIPAM brushes can act as macromolecular gates that modulate access to pores when temperature crosses the LCST, and previous work has reported strong conductance changes or rectification in PNIPAM-functionalized single nanopores[88]. However, the conductance behaviour of PNIPAM-grafted gold/silicon nitride nanopore arrays across different electrolytes, temperatures, and geometries has not been systematically mapped, particularly in direct comparison with non-responsive polymer controls such as short PEG brushes.

Scientific overview

This study examines ionic conductance through PNIPAM- and PEG-modified nanopore and nanopore arrays containing gold and silicon nitride. The core idea is that PNIPAM, by switching between swollen and collapsed states, can change the effective pore cross-section, thereby altering the measured conductance as temperature passes the LCST. In contrast, 2 kDa PEG does not undergo a structural transition in this temperature range and therefore provides a control where conductance changes should mainly follow the known temperature dependence of bulk electrolyte conductivity.

Single pores, 36-pore arrays, and 225-pore sparse arrays are compared in phosphate-buffered saline (PBS) and 1 M KCl to assess how ionic strength and solvent quality influence both polymer conformation and wetting. I–V curves are recorded at room temperature and at 40 °C, and conductance G is taken from the slope. The aim is to disentangle three contributions to the observed changes in G: (i) bulk conductivity[*] of the electrolyte, (ii) polymer-specific effects from PNIPAM, and (iii) artifacts due to incomplete or unstable wetting and geometry-dependent averaging.

---

[*] **Conductivity increases with increase in temperature**

Purpose and research questions

The purpose of this work is to determine how PNIPAM brushes on nanopores influence ionic conductance as a function of temperature, and under which conditions the response can be interpreted as genuine thermoresponsive gating rather than as a consequence of bulk or experimental effects. Specifically, it asks:

1. What is the conductance response at the PNIPAM collapsed state, and is this response reproducible under repeated cycles?
2. How does the ionic conductance of PNIPAM grafted nanopores depend on electrolyte concentration and ionic strength?
3. In nanopore arrays, how does access resistance contribute to the total conductance, and how is this contribution influenced by pore density and interpore spacing (i.e., how closely the pores are packed)?
4. What wetting protocols and surface/solution conditions are required to ensure complete and stable wetting of PNIPAM modified nanopores?

These questions connect to RQ4 in the Scope, which asks how thermoresponsive PNIPAM-grafted nanostructures influence ionic transport and when they provide reliable conductance readouts.

Methods

Conductance experiments* used electron-beam-defined nanopore arrays in membranes comprising a silicon nitride and gold film. The set of structures included single pores, 36-pore arrays, and 225-pore sparse arrays, allowing comparison between single-pore responses and ensemble averages.

PNIPAM brushes were grafted to the gold surface by surface-initiated polymerization, using initiator chemistries analogous to those in the nanowell experiments. In parallel, 2 kDa PEG brushes were grafted as non-responsive controls. PEG in this molecular-weight range is hydrophilic and protein-resistant, and its conductance response is expected to be dominated by the electrolyte rather than by polymer reorganization. Comparing PNIPAM and

---

[*] **Ion conductance studies test how PNIPAM modulates ionic transport across LCST.**

PEG coatings on otherwise similar structures makes it possible to separate polymer-specific gating from generic temperature effects.

Electrolytes and measurement conditions

Ionic conductance was measured in PBS and 1 M KCl. PBS provides a moderate ionic strength compatible with biological measurements and is less likely to strongly suppress PNIPAM's thermoresponse, whereas 1 M KCl represents a high-ionic-strength, potentially poorer solvent for the polymer. For each sample and condition, I–V curves were recorded at room temperature and 40 °C; conductance G was obtained from linear fits, and repeated measurements were used to assess stability.

Expected results and main findings

In our measurements, 1× PBS yielded more stable current traces than 1 M KCl*, and it also provides a more physiologically relevant ionic environment due to its near-physiological ionic strength and composition ($\sim$0.15 M total salts, pH $\approx$ 7.4). Control experiments with 2 kDa PEG polymer brushes showed conductance that was insensitive to temperature as expected for a non-responsive polymer.

In 1 M KCl, the ionic conductance through PNIPAM-coated nanostructures exhibited unstable and non-reproducible behaviour across both the collapsed and extended PNIPAM brush states. This behaviour can be understood within the framework of polymer brush scaling theory and the thermodynamics of polymer–solvent interactions.

According to the Alexander–de Gennes scaling theory, the key variables have the following physical meaning. Here, H denotes the polymer brush height, i.e. the average distance that the chains extend from the grafting surface into the solvent. N is the degree of polymerization and measures the number of monomer units per chain, and thus sets the maximum available contour length. σ denotes the grafting density, expressed as the number of chains per unit area of the surface; higher σ means that neighbouring chains are more crowded and must stretch away from the surface to avoid overlap. Finally, χ is the Flory–Huggins interaction parameter that quantifies solvent quality: $\chi < 0.5$ corresponds to a good solvent

---

* **PBS provides a more stable and physiologically relevant conductance environment**

with favourable monomer–solvent interactions, $\chi = 0.5$ to theta conditions, and $\chi > 0.5$ to a poor solvent where monomer–monomer contacts are energetically preferred. In a good solvent ($\chi < 0.5$), the brush is swollen with $H \propto N\sigma^{1/3}$ and in a poor solvent ($\chi > 0.5$), the brush collapses, and the scaling transitions to $H \propto N\sigma$, with the chains forming a dense, pancake-like layer. The transition between these regimes is governed by the balance between the entropic cost of chain stretching and the enthalpic gain from monomer–monomer contacts in a poor solvent environment.

High salt concentrations[*] are known to deteriorate the solvent quality for PNIPAM and to lower its lower critical solution temperature (LCST) via Hofmeister-type "salting-out" effects. Molecular dynamics and scattering studies have shown that salts such as NaCl or KCl can reduce the LCST of PNIPAM solutions by several tens of degrees, promoting chain collapse and dehydration even close to room temperature. Under our experimental conditions, 1 M KCl therefore likely places the PNIPAM brushes in an effectively poor-solvent environment, shifting the LCST far below the studied temperature range and driving the brushes into a collapsed or near-collapsed state regardless of temperature. This would largely suppress the thermally triggered conformational transition that underpins the intended gating mechanism, which is consistent with the observed non-ideal and irreproducible conductance behaviour in 1 M KCl[89].

In contrast, measurements in phosphate-buffered saline (PBS, 1×) showed improved signal stability compared to 1 M KCl, suggesting that the lower ionic strength provides more favourable conditions for observing the thermoresponsive behaviour of PNIPAM brushes. PBS has an ionic strength and composition closer to those typically used to characterize PNIPAM LCST in aqueous solution, reducing salt-induced collapse and allowing the polymer chains to remain more hydrated below the LCST. Under these conditions, the brushes can respond more fully to temperature changes, which is expected to produce more pronounced and reproducible differences in conductance between the extended and collapsed states. However, additional measurements as a function of temperature in PBS are required

---

[*] **High ionic strength electrolytes are poor solvents for PNIPAM**

to conclusively establish the magnitude and reproducibility of the conductance modulation between the thermally defined states.

Control experiments with PEG

Conductance measurements on 2 kDa PEG-modified nanostructures were conducted at room temperature and 40 °C for comparison with a non-responsive polymer coating. PEG is a non-thermoresponsive polymer that does not undergo a conformational transition in this temperature range, and therefore any changes in conductance observed in PEG-modified structures can be attributed solely to non-specific effects such as instrumental drift or the intrinsic temperature dependence of the electrolyte conductivity.

The conductance measurements on PEG-modified[*] nanostructures showed an increase in conductance at 40°C compared to room temperature. This increase is not indicative of any polymer-mediated gating effect but rather corresponds to the well-established temperature dependence of the bulk electrolyte conductivity. The conductivity of aqueous inorganic electrolyte solutions increases with temperature at a rate of approximately 2% per °C at room temperature, due to the combined effects of increased ion mobility (reduced solvent viscosity) and, at high concentrations, the weakening of ion-pair associations with increasing temperature. At high electrolyte concentrations such as 1 M KCl, this temperature dependence is particularly pronounced, as the number of free ions increases with temperature due to the dissociation of ion pairs. For a temperature increase from room temperature (~22–25°C) to 40°C, a conductance increase of approximately 30–36% would be expected from the bulk conductivity change alone[90]. The observation that the conductance increases in PEG-modified structures at 40°C is quantitatively consistent with the expected bulk conductivity change confirms that PEG brushes do not introduce any additional temperature-dependent modulation of ion transport. This result validates that PEG-modified nanostructures serve as an appropriate control: the PEG layer remains structurally invariant with temperature, and measured conductance changes reflect only the intrinsic temperature dependence of the electrolyte solution.

---

[*] **PBS provides a more stable and physiologically relevant conductance environment**

Chapter 5

Conclusion and Outlook

5.1 Concluding remarks

The event-frequency study demonstrates that analyte concentration can be determined directly from the dependence of nanopore event frequency on applied voltage, without external calibration or additional reference species. By introducing robust signal-processing algorithms to stabilize the baseline and accurately count events up to 1 V, it establishes event frequency as a quantitative observable and provides practical guidance for designing high-voltage nanopore experiments.

The electric-field study shows that the intense DC field inside solid-state nanopores can drastically shorten the lifetime of even the strongest protein–ligand interaction, biotin–avidin, by at least four orders of magnitude. This reveals that the nanopore environment is not passive: field-driven forces can dissociate surface-bound complexes on the timescale of minutes and may render affinity-based sensing quantitatively unreliable if such effects are ignored.

Taken together[*], the two papers conclude that solid-state nanopores are powerful, calibration-free electrical sensors for concentration readout, but that their extreme fields can strongly perturb biomolecular interactions, which must be explicitly accounted for in any bioanalytical applications.

---

[*] **The thesis establishes nanopores as quantitative sensors while showing that their electric field can perturb biology.**

5.2 Outlook

Future work on the PNIPAM enzyme confinement system will focus on achieving single-enzyme trapping by tuning the enzyme concentration. An important next step is to systematically tune the enzyme loading conditions so that most active nanowells contain zero or one enzyme molecule. This will require lowering the enzyme concentration to 1uM, while keeping the signal-to-noise ratio high enough to detect single-enzyme activity. Alongside, the work also focuses on trapping the enzymes without adsorbing onto the pore walls. Together, it would establish design rules for choosing substrate and concentration conditions that bring the PNIPAM-gated platform from enzyme clusters toward a robust single-enzyme regime.

On the ionic transport side, future experiments will focus exclusively on low ionic strength electrolytes, as high ionic strength electrolytes are poor solvents for PNIPAM brushes and suppresses their thermoresponsive behaviour. Both single nanopores and multiple-pore arrays will be tested in different electrolytes to establish reproducible, temperature-dependent conductance changes between the extended and collapsed PNIPAM states. In parallel, the wetting properties of PNIPAM-modified nanopores will be compared with those of 2 kDa PEG-modified nanopores. Since PNIPAM undergoes a hydrophilic-to-hydrophobic transition at the LCST while PEG remains hydrophilic across the same temperature range, comparing the two polymer systems will help disentangle the contributions of polymer conformation to the observed conductance changes and surface wettability.

By grafting responsive polymers onto nanostructures, one could create adaptive nanoscale environments that respond to chemical or physical cues and actively regulate molecular access and transport*. This represents a path toward multifunctional solid-state nanodevices that combine electrical sensing with dynamic control over the local biomolecular environment.

---

* **Future work moves toward single-enzyme trapping and ion conductance studies with responsive polymer gates.**

Bibliography

1. Electrolyte Balance. in *Anatomy and Physiology 2e*.
2. Jurkat-Rott, K. & Lehmann-Horn, F. Ion Channels and Electrical Properties of Skeletal Muscle.
3. Qiu, Q., Yang, M., Gong, D., Liang, H. & Chen, T. Potassium and calcium channels in different nerve cells act as therapeutic targets in neurological disorders. *Neural Regeneration Research* **20**, 1258–1276 (2025).
4. Kuo, I. Y. & Ehrlich, B. E. Signaling in Muscle Contraction. *Cold Spring Harb Perspect Biol* **7**, a006023 (2015).
5. Chapter Four: Principles of Fluids and Electrolytes. in *Intravenous (IV) Therapy for Practical Nurses*.
6. Nicholls, D. G. Mitochondrial function and dysfunction in the cell: its relevance to aging and aging-related disease. *The International Journal of Biochemistry & Cell Biology* **34**, 1372–1381 (2002).
7. Shin, S., Kim, J., Song, E., Han, S. & Hohng, S. Analytical techniques for nucleic acid and protein detection with single-molecule sensitivity. *Exp Mol Med* **57**, 938–949 (2025).
8. Casas, M. & Dickson, E. J. Channels, Transporters, and Receptors at Membrane Contact Sites. *Contact* **7**, 25152564241305593 (2024).
9. Zhou, H.-X. Influence of crowded cellular environments on protein folding, binding, and oligomerization: Biological consequences and potentials of atomistic modeling. *FEBS Letters* **587**, 1053–1061 (2013).
10. Dekker, C. Solid-state nanopores. *Nature Nanotech* **2**, 209–215 (2007).

11. Luo, Y. *et al.* Resolving Molecular Heterogeneity with Single-Molecule Centrifugation. *J. Am. Chem. Soc.* **145**, 3276–3282 (2023).
12. Assadipapari, M. *et al.* Tracking single-molecule ferritin reassembly and disassembly using polymer-coated nanopores. *Nanoscale* **18**, 1045–1054 (2026).
13. Deniz, A. A., Mukhopadhyay, S. & Lemke, E. A. Single-molecule biophysics: at the interface of biology, physics and chemistry. *J. R. Soc. Interface.* **5**, 15–45 (2008).
14. Smiley, R. D. & Hammes, G. G. Single Molecule Studies of Enzyme Mechanisms. *Chem. Rev.* **106**, 3080–3094 (2006).
15. Shrikrishna, N. S. & Gandhi, S. Nanopore-based sensing for biomarker detection: from fundamental principles to translational diagnostics. *J Nanobiotechnol* **23**, 663 (2025).
16. Bahrami, A., Doğan, F., Japrung, D. & Albrecht, T. Solid-state nanopores for biosensing with submolecular resolution. *Biochemical Society Transactions* **40**, 624–628 (2012).
17. Hille, B. *Ion Channels of Excitable Membranes*. (Sinauer Assoc, Sunderland, Mass, 2001).
18. Lodish, H. *et al. Molecular Cell Biology*. (macmillan learning, Austin Boston New York Plymouth, 2021).
19. Stoddart, D. *et al.* Functional truncated membrane pores. *Proc. Natl. Acad. Sci. U.S.A.* **111**, 2425–2430 (2014).
20. Pavlenok, M. & Niederweis, M. Hetero-oligomeric MspA pores in *Mycobacterium smegmatis*. *FEMS Microbiology Letters* **363**, fnw046 (2016).
21. Cao, C. *et al.* Single-molecule sensing of peptides and nucleic acids by engineered aerolysin nanopores. *Nat Commun* **10**, 4918 (2019).

22. Wei, X. *et al.* Engineering Biological Nanopore Approaches toward Protein Sequencing. *ACS Nano* **17**, 16369–16395 (2023).

23. Bhatti, H. *et al.* Recent advances in biological nanopores for nanopore sequencing, sensing and comparison of functional variations in MspA mutants. *RSC Adv.* **11**, 28996–29014 (2021).

24. Anton, J. S. *et al.* Aerolysin Nanopore Structures Revealed at High Resolution in a Lipid Environment. *J. Am. Chem. Soc.* **147**, 4984–4992 (2025).

25. Mayer, S. F., Cao, C. & Dal Peraro, M. Biological nanopores for single-molecule sensing. *iScience* **25**, 104145 (2022).

26. Zhou, W., Guo, Y., Guo, W. & Qiu, H. High-Resolution and Low-Noise Single-Molecule Sensing with Bio-Inspired Solid-State Nanopores. *J. Phys. Chem. Lett.* **15**, 5556–5563 (2024).

27. Akabirov, K. *et al.* The evolution of nanopore measurements: from biological out-of-plane pores to plastic in-plane pores. *Lab Chip* **26**, 1709–1738 (2026).

28. Zvuloni, E., Zrehen, A., Gilboa, T. & Meller, A. Fast and Deterministic Fabrication of Sub-5 Nanometer Solid-State Pores by Feedback-Controlled Laser Processing. *ACS Nano* **15**, 12189–12200 (2021).

29. Wen, C. Solid-State Nanopores for Sensing. From Theory to Applications. (Uppsala University, Uppsala, 2019).

30. Bell, N. A. W. & Keyser, U. F. Nanopores formed by DNA origami: A review. *FEBS Letters* **588**, 3564–3570 (2014).

31. Liu, M., Li, J. & Tan, C. S. Unlocking the Power of Nanopores: Recent Advances in Biosensing Applications and Analog Front-End. *Biosensors* **13**, 598 (2023).

32. Kasianowicz, J. J., Brandin, E., Branton, D. & Deamer, D. W. Characterization of individual polynucleotide molecules using a membrane channel. *Proc. Natl. Acad. Sci. U.S.A.* **93**, 13770–13773 (1996).

33. Rostovtseva, T. K., Komarov, A., Bezrukov, S. M. & Colombini, M. Dynamics of Nucleotides in VDAC Channels: Structure-Specific Noise Generation. *Biophysical Journal* **82**, 193–205 (2002).

34. Braha, O. *et al.* Designed protein pores as components for biosensors. *Chemistry & Biology* **4**, 497–505 (1997).

35. De Zoysa, R. S. S., Krishantha, D. M. M., Zhao, Q., Gupta, J. & Guan, X. Translocation of single-stranded DNA through the α-hemolysin protein nanopore in acidic solutions. *Electrophoresis* **32**, 3034–3041 (2011).

36. Butler, T. Z., Gundlach, J. H. & Troll, M. Ionic Current Blockades from DNA and RNA Molecules in the α-Hemolysin Nanopore. *Biophysical Journal* **93**, 3229–3240 (2007).

37. Silva, A. *et al.* Stochastic Sensing of Organotin Compounds with Alpha-Hemolysin Nanopore. *J. Braz. Chem. Soc.* https://doi.org/10.21577/0103-5053.20230127 (2024) doi:10.21577/0103-5053.20230127.

38. Winters-Hilt, S. The α-Hemolysin nanopore transduction detector – single-molecule binding studies and immunological screening of antibodies and aptamers. *BMC Bioinformatics* **8**, S9 (2007).

39. Li, J. *et al.* Ion-beam sculpting at nanometre length scales. *Nature* **412**, 166–169 (2001).

40. Fürjes, P. *et al.* Effects of the Focused Ion Beam Parameters on Nanopore Milling in Solid State Membranes. *Procedia Engineering* **47**, 684–687 (2012).

41. Storm, A. J., Chen, J. H., Ling, X. S., Zandbergen, H. W. & Dekker, C. Fabrication of solid-state nanopores with single-nanometre precision. *Nature Mater* **2**, 537–540 (2003).
42. Kwok, H., Briggs, K. & Tabard-Cossa, V. Nanopore Fabrication by Controlled Dielectric Breakdown. *PLoS ONE* **9**, e92880 (2014).
43. Lee, K. *et al.* Recent Progress in Solid-State Nanopores. *Advanced Materials* **30**, 1704680 (2018).
44. He, Y., Tsutsui, M., Zhou, Y. & Miao, X.-S. Solid-state nanopore systems: from materials to applications. *NPG Asia Mater* **13**, 48 (2021).
45. Cairns-Gibson, D. F. & Cockroft, S. L. Functionalised nanopores: chemical and biological modifications. *Chem. Sci.* **13**, 1869–1882 (2022).
46. Emilsson, G. *et al.* Polymer brushes in solid-state nanopores form an impenetrable entropic barrier for proteins. *Nanoscale* **10**, 4663–4669 (2018).
47. Kowalczyk, S. W., Grosberg, A. Y., Rabin, Y. & Dekker, C. Modeling the conductance and DNA blockade of solid-state nanopores. *Nanotechnology* **22**, 315101 (2011).
48. Hall, J. E. Access resistance of a small circular pore. *The Journal of general physiology* **66**, 531–532 (1975).
49. Sahu, S. & Zwolak, M. Maxwell-Hall access resistance in graphene nanopores. *Phys. Chem. Chem. Phys.* **20**, 4646–4651 (2018).
50. Baldock, H. C. M. & Huang, D. M. Revisiting the access conductance of a nanopore in a charged membrane. *The Journal of Chemical Physics* **163**, 224706 (2025).
51. Cain, D., Cao, E., Vlassiouk, I., Schäffer, T. E. & Siwy, Z. S. Ion concentration polarization causes a nearly pore-length-independent conductance of nanopores. *Faraday Discuss.* **257**, 344–359 (2025).

52. Yeh, H.-C., Chang, C.-C. & Yang, R.-J. Electro-osmotic pumping and ion-concentration polarization based on conical nanopores. *Phys. Rev. E* **91**, 062302 (2015).

53. Smeets, R. M. M. *et al.* Salt Dependence of Ion Transport and DNA Translocation through Solid-State Nanopores. *Nano Lett.* **6**, 89–95 (2006).

54. Wanunu, M., Morrison, W., Rabin, Y., Grosberg, A. Y. & Meller, A. Electrostatic focusing of unlabelled DNA into nanoscale pores using a salt gradient. *Nature Nanotech* **5**, 160–165 (2010).

55. Aarts, M. *et al.* Ion Current Rectification and Long-Range Interference in Conical Silicon Micropores. *ACS Appl. Mater. Interfaces* **14**, 56226–56236 (2022).

56. Ma, L. *et al.* Modulation of Ionic Current Rectification in Ultrashort Conical Nanopores. *Anal. Chem.* **92**, 16188–16196 (2020).

57. Valiskó, M. *et al.* Multiscale analysis of the effect of surface charge pattern on a nanopore's rectification and selectivity properties: From all-atom model to Poisson-Nernst-Planck. *The Journal of Chemical Physics* **150**, 144703 (2019).

58. Järlebark, J., Liu, W., Shaji, A., Sha, J. & Dahlin, A. Solid-State Nanopore Sensors: Analyte Quantification by Event Frequency Analysis at High Voltages. *Anal. Chem.* **97**, 4359–4364 (2025).

59. Ando, G., Hyun, C., Li, J. & Mitsui, T. Directly Observing the Motion of DNA Molecules near Solid-State Nanopores. *ACS Nano* **6**, 10090–10097 (2012).

60. Grosberg, A. Y. & Rabin, Y. DNA capture into a nanopore: Interplay of diffusion and electrohydrodynamics. *The Journal of Chemical Physics* **133**, 165102 (2010).

61. Chinappi, M., Yamaji, M., Kawano, R. & Cecconi, F. Analytical Model for Particle Capture in Nanopores Elucidates Competition among Electrophoresis, Electroosmosis, and Dielectrophoresis. *ACS Nano* **14**, 15816–15828 (2020).

62. Wong, C. T. A. & Muthukumar, M. Polymer capture by electro-osmotic flow of oppositely charged nanopores. *The Journal of Chemical Physics* **126**, 164903 (2007).
63. Rowghanian, P. & Grosberg, A. Y. Electrophoretic capture of a DNA chain into a nanopore. *Phys. Rev. E* **87**, 042722 (2013).
64. Buyukdagli, S. & Ala-Nissila, T. Controlling polymer capture and translocation by electrostatic polymer-pore interactions. *The Journal of Chemical Physics* **147**, 114904 (2017).
65. Xu, X. *et al.* Recent Advances in Antifouling Surface Polymer Brushes. *ACS Appl. Polym. Mater.* **6**, 1–27 (2024).
66. Lokesh, M. G. & Tiwari, A. K. A concise review on polymer brushes and its interaction with surfactants: An approach towards smart materials. *Journal of Molecular Liquids* **407**, 125168 (2024).
67. Ma, S., Zhang, X., Yu, B. & Zhou, F. Brushing up functional materials. *NPG Asia Mater* **11**, 24 (2019).
68. Postma, E. J., Scheres, L., De Beer, S., Kuzmyn, A. R. & Zuilhof, H. Functionalized Antifouling Polymer Brushes for Biospecific Surfaces. *Adv Materials Inter* **12**, 2400955 (2025).
69. Milner, S. T. Polymer Brushes. *Science* **251**, 905–914 (1991).
70. De Gennes, P. G. Polymers at an interface; a simplified view. *Advances in Colloid and Interface Science* **27**, 189–209 (1987).
71. Alexander, S. Adsorption of chain molecules with a polar head a scaling description. *J. Phys. France* **38**, 983–987 (1977).
72. Hildebrandt, M. *et al.* Investigation of Roughness Correlation in Polymer Brushes via X-ray Scattering. *Polymers* **12**, 2101 (2020).

73. Zoppe, J. O. *et al.* Surface-Initiated Controlled Radical Polymerization: State-of-the-Art, Opportunities, and Challenges in Surface and Interface Engineering with Polymer Brushes. *Chem. Rev.* **117**, 1105–1318 (2017).

74. Kim, M., Schmitt, S., Choi, J., Krutty, J. & Gopalan, P. From Self-Assembled Monolayers to Coatings: Advances in the Synthesis and Nanobio Applications of Polymer Brushes. *Polymers* **7**, 1346–1378 (2015).

75. Zdyrko, B. & Luzinov, I. Polymer Brushes by the "Grafting to" Method. *Macromol. Rapid Commun.* **32**, 859–869 (2011).

76. Hüküm Özkan, K., Mutlutürk, E., DemiR Çalişkan, T. & Çaykara, T. Synthesis of Polymer Brushes by Surface-Initiated Controlled/Living Free Radical Polymerization Techniques. *Hacettepe Journal of Biology and Chemistry* **48**, 395–405 (2020).

77. Abdulhalim, I., Zourob, M. & Lakhtakia, A. Surface Plasmon Resonance for Biosensing: A Mini-Review. *Electromagnetics* **28**, 214–242 (2008).

78. Andersson, J., Svirelis, J., Ferrand-Drake Del Castillo, G., Sannomiya, T. & Dahlin, A. Surface plasmon resonance sensing with thin films of palladium and platinum – quantitative and real-time analysis. *Phys. Chem. Chem. Phys.* **24**, 4588–4594 (2022).

79. Andersson, J. *et al.* Polymer Brushes on Silica Nanostructures Prepared by Aminopropylsilatrane Click Chemistry: Superior Antifouling and Biofunctionality. *ACS Appl. Mater. Interfaces* **15**, 10228–10239 (2023).

80. Charron, M., Briggs, K., King, S., Waugh, M. & Tabard-Cossa, V. Precise DNA Concentration Measurements with Nanopores by Controlled Counting. *Anal. Chem.* **91**, 12228–12237 (2019).

81. Klughammer, N. & Dekker, C. Palladium zero-mode waveguides for optical single-molecule detection with nanopores. *Nanotechnology* **32**, 18LT01 (2021).
82. Svirelis, J. *et al.* Stable trapping of multiple proteins at physiological conditions using nanoscale chambers with macromolecular gates. *Nat Commun* **14**, 5131 (2023).
83. Harrisson, S., Whitfield, R., Anastasaki, A. & Matyjaszewski, K. Atom transfer radical polymerization. *Nat Rev Methods Primers* **5**, 2 (2025).
84. Shivapooja, P., Ista, L. K., Canavan, H. E. & Lopez, G. P. ARGET–ATRP Synthesis and Characterization of PNIPAAm Brushes for Quantitative Cell Detachment Studies. *Biointerphases* **7**, 32 (2012).
85. Maksimainen, M. M., Lampio, A., Mertanen, M., Turunen, O. & Rouvinen, J. The crystal structure of acidic β-galactosidase from Aspergillus oryzae. *International Journal of Biological Macromolecules* **60**, 109–115 (2013).
86. Wahba, M. I. Thermostabilization of *Aspergillus oryzae* β- D -galactosidase. *Biotech and App Biochem* **63**, 546–552 (2016).
87. Guidini, C. Z., Fischer, J., Santana, L. N. S., Cardoso, V. L. & Ribeiro, E. J. Immobilization of Aspergillus oryzae β-galactosidase in ion exchange resins by combined ionic-binding method and cross-linking. *Biochemical Engineering Journal* **52**, 137–143 (2010).
88. Yameen, B. *et al.* Ionic Transport Through Single Solid-State Nanopores Controlled with Thermally Nanoactuated Macromolecular Gates. *Small* **5**, 1287–1291 (2009).
89. Laktionov, M. Y., Zhulina, E. B., Richter, R. P. & Borisov, O. V. Polymer Brush in a Nanopore: Effects of Solvent Strength and Macromolecular Architecture Studied by Self-Consistent Field and Scaling Theory. *Polymers* **13**, 3929 (2021).

90. Zhang, W., Chen, X., Wang, Y., Wu, L. & Hu, Y. Experimental and Modeling of Conductivity for Electrolyte Solution Systems. *ACS Omega* **5**, 22465–22474 (2020).